A parameterization of local and remote tidal mixing

C. de Lavergne,[1*] C. Vic,[2] G. Madec,[1,3] F. Roquet,[4]
A. F. Waterhouse,[5] C. B. Whalen,[6] Y. Cuypers,[1]
P. Bouruet-Aubertot,[1] B. Ferron,[2] T. Hibiya[7]

[1]LOCEAN Laboratory, Sorbonne Université-CNRS-IRD-MNHN,
Paris F-75005, France
[2]LOPS Laboratory, UBO-IFREMER-CNRS-IRD,
Plouzané, France
[3]LJK Laboratory, Université Grenoble Alpes-INRIA-CNRS,
Grenoble, France
[4]Department of Marine Sciences, University of Gothenburg,
S-405 30 Gothenburg, Sweden
[5]Scripps Institution of Oceanography, University of California,
La Jolla, California
[6]Applied Physics Laboratory, University of Washington,
Seattle, Washington
[7]Department of Earth and Planetary Science, Graduate School of Science,
The University of Tokyo, Tokyo, Japan

[*]To whom correspondence should be addressed; e-mail: casimir.delavergne@locean.upmc.fr

Main points

- A global three-dimensional map of mixing induced by internal tides is presented.
- The map can serve as a comprehensive and energy-constrained tidal mixing parameterization in global ocean models.
- The map compares well to available microstructure and upper-ocean finestructure mixing estimates.

Abstract

Vertical mixing is often regarded as the Achilles' heel of ocean models. In particular, few models include a comprehensive and energy-constrained parameterization of mixing by internal ocean tides. Here, we present an energy-conserving mixing scheme which accounts for the local breaking of high-mode internal tides and the distant dissipation of low-mode internal tides. The scheme relies on four static two-dimensional maps of internal tide dissipation, constructed using mode-by-mode Lagrangian tracking of energy beams from sources to sinks. Each map is associated with a distinct dissipative process and a corresponding vertical structure. Applied to an observational climatology of stratification, the scheme produces a global three-dimensional map of dissipation which compares well with available microstructure observations and with upper-ocean finestructure mixing estimates. This relative agreement, both in magnitude and spatial structure across ocean basins, suggests that internal tides underpin most of observed dissipation in the ocean interior at the global scale. The proposed parameterization is therefore expected to improve understanding, mapping and modelling of ocean mixing.

Plain Language Summary

When tidal ocean currents flow over bumpy seafloor, they generate internal tidal waves. Internal waves are the subsurface analogue of surface waves that break on beaches. Like surface waves, internal tidal waves often become unstable and break into turbulence. This turbulence is a primary cause of mixing between stacked ocean layers, which is in turn a key contributor to ocean currents and biology and a key ingredient of computer models of the global ocean. In this article, a three-dimensional global map of mixing induced by internal tidal waves is presented. This map incorporates a large variety of energy pathways from the generation of tidal waves to turbulence, accounting for the conservation of energy. The map is compared to available observations of turbulence across the globe and found to reproduce with good fidelity the main patterns identified in observations. This relatively good agreement suggests that internal tidal waves are the main source of turbulence in the subsurface ocean, and implies that the map may serve a range of applications. In particular, the three-dimensional map provides an efficient and realistic means to represent mixing by internal tidal waves in global ocean models.

1. Introduction

When tidal currents flow over sloping topography, they generate inertio-gravity waves called internal tides (Bell 1975). Internal tides have long been suspected to play an important role in mixing the deep ocean (Munk 1966). Accumulating observations from the past three decades suggest that tides power much of the small-scale turbulence responsible for irreversible mixing, not only in the deep ocean (Polzin et al. 1997, Ledwell et al. 2000) but also in the upper ocean (Hibiya and Nagasawa 2004, Kunze et al. 2006, Polzin 2009, Whalen et al. 2012, Kunze 2017). However, mapping tidal mixing at the global scale has proven arduous because of the difficulty in measuring small-scale turbulence and in attributing the observed turbulence to specific dissipation pathways (Waterhouse et al. 2014, MacKinnon et al. 2017). As a result, extant parameterizations of tidal mixing suffer from substantial simplifications and uncertainties in the specified distribution of internal tide energy dissipation. These uncertainties limit in turn our understanding of the drivers, structure and climatic functions of the overturning circulation (Sigman et al. 2010, de Lavergne et al. 2016, Melet et al. 2016).

Internal tides radiate from the seafloor with a variety of spatial scales. Small-scale internal tides, referred to as high-mode internal tides, tend to break into small-scale turbulence close to generation site (St Laurent and Garrett 2002). By contrast, large-scale or low-mode internal tides can travel hundreds to thousands of kilometers and fuel dissipation remote from generation site (Dushaw et al. 1995, Ray and Mitchum 1996). Most tidal mixing parameterizations in use in Ocean General Circulation Models (OGCMs) only consider high-mode internal tides. They rely on a map of internal tide generation and posit that one-third of this energy source feeds high-mode waves that dissipate in the local water column (St Laurent et al. 2002). The remaining two-thirds of power input are ignored or surmised to participate in sustaining a con-

stant background diffusivity of order 10^{-5} m^2 s^{-1} (Simmons et al. 2004). This approach has two principal limitations: (i) the fraction of local dissipation is not uniform and actually depends on resolution and location (St Laurent and Nash 2004, Falahat et al. 2014a, Vic et al. 2019); (ii) constant background diffusivities disallow energy conservation and do not do justice to observed patterns of mixing rates (de Lavergne et al. 2019).

Several recent studies tackled the limitation (ii) by explicitly including mixing powered by low-mode internal tides. Oka and Niwa (2013) employed a static horizontal map of low-mode dissipation derived from high-resolution numerical experiments (Niwa and Hibiya 2011). Assuming that this dissipation is uniform in the vertical, they assessed the impact of adding remote tidal mixing in an OGCM. Eden and Olbers (2014) proposed an interactive parameterization of low-mode energy propagation and dissipation. They introduced an equation for the evolution of low-mode energy within an OGCM. A map of low-mode internal tide generation, parameterized attenuation rates and a simple model for the vertical dependence of dissipation then allow solving for the evolving tidal mixing rates. These studies demonstrate the feasibility and importance of replacing background diffusivities by an explicit parameterization of remote tidal mixing. Further advance requires improvements in the realism of the modelled distribution of internal wave energy loss. The vertical structure of dissipation needs particular attention, as it is crucial for ocean ventilation and as it depends on the process causing dissipation (de Lavergne et al. 2016, Melet et al. 2016).

To accurately parameterize mixing energized by low-mode internal tides, it is thus necessary to track where and how they dissipate. Using Lagrangian tracking of internal tide energy beams through observed stratification, de Lavergne et al. (2019) recently estimated column-integrated internal tide dissipation rates decomposed into contributing processes. Here, we make use of

these horizontal maps and of historical microstructure observations to propose a comprehensive and energy-constrained parameterization of tidal mixing. The parameterization explicitly accounts for the local and remote dissipation of internal tides and obviates assumptions about the fraction of local dissipation. It relies on four static maps of column-integrated dissipation, each associated with a distinct process and related vertical structure (section 2). To gauge the realism of the parameterization, we apply it to an observational hydrographic climatology, and compare the obtained three-dimensional distribution of mixing to a compilation of observational mixing estimates (section 3). We then document the inferred global budget of internal tide-induced dissipation (section 4) and conclude with a summary of implications and limitations of the analysis (section 5).

2. Process-dependent vertical structures

The vertical mode of internal tides is a key determinant of their propagation and dissipation characteristics (Olbers 1976). The lowest modes have elevated group speeds and relatively slow rates of attenuation by wave-wave interactions. They consequently tend to lose much of their energy through interactions with topography (Kelly et al. 2013). Conversely, high vertical modes tend to lose most of their energy through wave-wave interactions within the near-local water column (Nikurashin and Legg 2011). These different fates of internal tides were mapped globally, for each mode and each of the main three tidal constituents (M_2, S_2 and K_1), using the following ingredients (Fig. 1; de Lavergne et al. 2019): (i) an observational climatology of stratification (Gouretski and Koltermann 2004); (ii) estimates of internal tide generation projected onto vertical modes (Falahat et al. 2014b, Melet et al. 2013a); (iii) simplified representations of energy sinks (Olbers 1983, Bühler and Holmes-Cerfon 2011, Hazewinkel and Winters 2011,

MacKinnon et al. 2013, Legg 2014); and (iv) a Lagrangian energy tracker.

Modes 6 and higher, which cumulate a power of 217 GW, were found to dissipate locally at the half-degree resolution of the calculation. These locally dissipating modes comprise modes 6 to 10 (115 GW; Falahat et al. 2014b) and much higher modes generated by abyssal hills (102 GW; Melet et al. 2013a). The dissipation of modes 1 to 5 was split into four processes: wave-wave interactions (521 GW), incidence on critical topographic slopes (128 GW), shoaling (95 GW) and scattering by abyssal hills (83 GW). Here we organize these contributions to the overall internal tide energy loss (1044 GW) into four components, based on expectations about induced vertical structures of turbulent kinetic energy production (Fig. 1):

- E_{wwi}: attenuation of low modes by wave-wave interactions;
- E_{sho}: direct breaking of low-mode waves through shoaling;
- E_{cri}: low-mode waves dissipating at critical slopes;
- E_{hil}: scattering of low-mode waves by abyssal hills and generation of high-mode waves by abyssal hills.

The four components are mapped in Fig. 2. Generation and scattering by abyssal hills (E_{hil}) is most intense along ridges of the Atlantic and Indian basins while non-negligible throughout most of the open ocean (Fig. 2d). Abyssal hills are dominant features of the ocean floor at horizontal scales within 10 km (Macdonald et al. 1996, Goff 2010). They are thought to be responsible for the bulk of bottom-intensified mixing above rough ridges (Polzin 2004, Muller and Bühler 2009, Nikurashin and Legg 2011, Lefauve et al. 2015). The remaining three components encapsulate the dissipation of the first 10 vertical modes (Fig. 2a-c). Modes 6 to 10 are assumed to dissipate through wave-wave interactions (E_{wwi}) only, consistent with the over-

whelming contribution (99%) of this process to mode 5 dissipation (de Lavergne et al. 2019). E_{wwi} features widespread, strong depth-integrated dissipation and dominates the overall budget (Fig. 2a). A floor of 10^{-5} W m^{-2} was imposed on E_{wwi} to maintain a minimal amount of mixing poleward of the S_2 turning latitude (85.8°); this floor increased total dissipation by 0.1 GW. Shoaling (E_{sho}) mostly acts at the shelf break and shoreward, so that the induced turbulence is confined to relatively shallow waters (Fig. 2b). Dissipation of low-mode waves impinging on critical topography (E_{cri}) occurs primarily at continental slopes (Fig. 2c).

Power contained in the four static maps must now be distributed in the vertical to obtain a three-dimensional distribution of the production rate of turbulent kinetic energy. In all the following, this rate will be denoted ϵ and referred to as *turbulence production* for brevity. Turbulence production can be related to diffusivity K_ρ, buoyancy frequency N and frictional heat production ϵ_ν through the simplified balance (Osborn 1980)

$$\epsilon = K_\rho N^2 + \epsilon_\nu \ . \tag{1}$$

Introducing the flux Richardson number or *mixing efficiency* R_f, the buoyancy flux term can be expressed as $K_\rho N^2 = R_f \epsilon$. The constant value $R_f = 1/6$ is generally assumed in stratified oceanic conditions (Gregg et al. 2018). R_f should be distinguished from the *flux coefficient* $\Gamma = K_\rho N^2/\epsilon_\nu = R_f/(1 - R_f)$, used to deduce K_ρ from microstructure measurements of ϵ_ν, and usually taken to be one-fifth.

a. Low-mode components

Observational and theoretical evidence indicates that turbulence production fuelled by the downscale cascade of low-mode wave energy through wave-wave interactions scales with the square

of the buoyancy frequency (Müller et al. 1986, Gregg 1989, Polzin et al. 1995, Polzin 2004). Accordingly, we define the local power density ϵ_{wwi} (with units of W kg^{-1}) as

$$\epsilon_{wwi} = \frac{E_{wwi}}{\rho} \frac{N^2}{\int N^2 dz}, \tag{2}$$

where ρ denotes the in-situ density, z height and $\int dz$ an integral over the full water column.

Shoaling-induced dissipation often occurs via direct breaking of low-mode waves, so that the dissipation structure roughly matches the profile of the wave energy, proportional to N (D'Asaro and Lien 2000, Legg 2014, Melet et al. 2016). We choose

$$\epsilon_{sho} = \frac{E_{sho}}{\rho} \frac{N}{\int N dz}. \tag{3}$$

Incidence on critical slopes triggers boundary turbulence along the slope (Eriksen 1982, Moum et al. 2002, Legg and Adcroft 2003, Nash et al. 2004). The along-slope concentration of dissipation is not easily mimicked in a coarsely-resolved ocean with step-like topography. To roughly capture the vertical extent and bottom-intensification of the dissipation, we use an exponential decay from the seafloor with an e-folding scale H_{cri} equal to the along-slope height difference (Fig. 3a). The height scale for a given grid column (i, j) is thus defined as the largest local topographic rise,

$$H_{cri}(i,j) = H(i,j) - \min\big(H(i+1,j), H(i-1,j), H(i,j+1), H(i,j-1)\big), \tag{4}$$

with $H > 0$ the bathymetry. Where the so defined H_{cri} is negative, it is set instead as the subgrid-scale maximum local topographic rise (see Appendix A in de Lavergne et al. 2019). Turbulence production is then given by

$$\epsilon_{cri} = \frac{E_{cri}}{\rho} \frac{\exp(-h_{ab}/H_{cri})}{H_{cri}(1 - \exp(-H/H_{cri}))}, \tag{5}$$

where h_{ab} denotes the height above bottom. This exponential vertical structure implies that the bulk of dissipation occurs along the slope, but that some dissipation reaches higher up, in accord with results of process studies (Legg and Adcroft 2003, Legg 2014).

b. Abyssal hills

Several vertical structures have been proposed for the dissipation of internal tides excited by abyssal hills (Polzin 2004, 2009, Melet et al. 2013b, Lefauve et al. 2015). To assess these structures, we focus on a densely sampled area of the eastern Brazil Basin: 21-22°S; 16-19°W. During two cruises of the Brazil Basin Trace Release Experiment (BBTRE), in 1996 and 1997, 51 microstructure profiles were collected in this area (Polzin et al. 1997). Following Polzin (2009), we first construct a composite profile of turbulence production for the region by averaging microstructure profiles in depth coordinate over the upper 3 km, and in height-above-bottom coordinate over the bottom 1.5 km. The factor $(1 - R_f)^{-1} = 6/5$ is used to convert from the measured viscous dissipation to turbulence production. The resulting 4.5 km deep profile, shown in Fig. 4, implies a depth-integrated power consumption of 5.5×10^{-3} W m^{-2}. Somewhat coincidentally, the predicted internal tide energy loss, $E_{tid} = E_{wwi} + E_{sho} + E_{cri} + E_{hil}$, averaged over the same area is 5.6×10^{-3} W m^{-2}. Only E_{hil} and E_{wwi} are important contributors here, amounting to 3.5×10^{-3} and 2.0×10^{-3} W m^{-2}, respectively.

Using a simplified theory for the decay of hill-generated internal tides within uniform stratification, Polzin (2004) predicted that turbulence production ϵ decreases with h_{ab} following

$$\epsilon = \frac{\epsilon_0}{(1 + h_{ab}/H_{bot})^2}, \tag{6}$$

where H_{bot} is a height scale that depends on bottom conditions. Given H_{bot} = 150 m and

$\epsilon_0 = 10^{-8}$ W kg^{-1}, this structure provides a good fit to the Brazil Basin composite microstructure profile within 1.5 km of the bottom (Polzin 2004). Here, we must express ϵ_{hil} as a function of the depth-integrated power E_{hil} instead of the bottom ϵ_0. To this end, we introduce the parameter r_{bot}, which represents the fraction of E_{hil} that dissipates close to the bottom, i.e., following equation (6). We obtain a best fit to the bottom-intensified portion of the composite microstructure profile using $r_{bot} = 0.86$, together with H_{bot} = 150 m (Fig. 4b). The remainder of the power, $(1 - r_{bot})E_{hil}$, feeds small-scale turbulence in the shallower portion of the water column. We choose to distribute this remainder as proportional to N^2, consistent with turbulence arising from weakly nonlinear wave-wave interactions (Polzin 2009). The complete parameterized vertical structure for ϵ_{hil} is thus given by

$$\epsilon_{hil} = \frac{E_{hil}}{\rho}\left[r_{bot}\frac{1}{(1+h_{ab}/H_{bot})^2}\left(\frac{1}{H}+\frac{1}{H_{bot}}\right) + (1-r_{bot})\frac{N^2}{\int N^2 dz}\right] \tag{7}$$

The factor $\frac{1}{H} + \frac{1}{H_{bot}}$ comes from normalization of the depth-integrated power. When adding ϵ_{wwi}, this parameterization tracks the observational profile over the full water column (Fig. 4c). Quantitatively, the percentage power contained in each 750-m layer of the parameterized profile is within 1% of its observational counterpart (Table 1).

We assess two alternative parameterizations (Fig. 4d-i; Lefauve et al. 2015, Melet et al. 2013b). They apply to ϵ_{hil} only (Fig. 4e,h), so that ϵ_{wwi} is distributed according to equation (2) in every $\epsilon_{hil} + \epsilon_{wwi}$ profile (Fig. 4f,i). Both parameterizations resort to a stratification-weighted height above bottom,

$$h_{wkb,m} = H\frac{\int_{-H}^{z} N^m dz}{\int_{-H}^{0} N^m dz}, \tag{8}$$

also known as Wentzel-Kramers-Brillouin stretching. Here m is an exponent equal to 1 (Fig. 4d) or 2 (Fig. 4g). Lefauve et al. (2015) proposed a profile of turbulence production proportional to $N^2 \exp(-h_{wkb,1}/H_L)$, where H_L is a height scale. As shown in Fig. 4f and Table 1, the best

fit obtained for H_L = 400 m is unsatisfactory within the bottom portion of the water column: the structure is strongly influenced by the local maximum in stratification near 3.7 km depth (Fig. 4a). Recasting the structure of Polzin (2009) in an energy-conserving form, Melet et al. (2013b) proposed a profile proportional to $N^2(1+h_{wkb,2}/H_M)^{-2}$, with H_M an appropriate decay scale. This structure provides a reasonable fit to the composite microstructure profile for H_M = 5 m (Fig. 4i and Table 1). However, turbulence production is underestimated at mid-depth, near the local minimum in stratification. On the whole, parameterization (7) best mimics the measured dissipation across the water column.

Parameterization (7) has an additional important characteristic: it ensures that near-bottom turbulence levels are decoupled from upper-ocean changes in stratification. This is not the case of structures proposed by Melet et al. (2013b) and Lefauve et al. (2015), according to which an increase in near-surface stratification implies a reduction of the power input to abyssal mixing. The latter behaviour is illustrated in Fig. 5 by applying the three parameterizations to climatological summer and winter profiles of stratification in the region 21-22°S; 16-19°W. In summer, larger buoyancy frequencies in the upper 400 m of the water column lead to a decrease of turbulence production in the bottom kilometer using the structure of Lefauve et al. (2015), and in the bottom grid cell using that of Melet et al. (2013b). A long-term increase in upper-ocean stratification, as may occur under a climate change scenario, would similarly drain mixing energy from the abyss. In contrast, parameterization (7) predicts unchanged abyssal mixing under unchanged abyssal conditions, as expected for turbulence driven by the rapid decay of bottom-generated small-scale internal tides (Polzin 2004, 2009).

Properties of parameterization (7) rely on the introduction of two adjustable parameters, H_{bot} and r_{bot}. These parameters are expected to vary geographically: more energetic or smaller scale

waves should decay more rapidly above the bottom, implying smaller H_{bot} or higher r_{bot} or both (Lefauve et al. 2015). Lefauve et al. (2015) found that internal tide energy dissipation above abyssal hills is largely shaped by the root-mean-square amplitude of internal tides at the bottom, A_{rms}. This characteristic wave amplitude is related to the power input E_{hil} and the mean local wavenumber of abyssal hills k_{hil} via the scaling[1] $A_{rms} \propto E_{hil}^{1/2} k_{hil}^{3/2}$. We mapped A_{rms} using k_{hil} estimated by Goff (2010). In general, A_{rms} decays away from the crest of the main mid-ocean ridges (Fig. 3c). The eastern Brazil Basin has relatively short-scale abyssal hills and relatively large A_{rms} (Fig. 6). Hence, on average, turbulence induced by abyssal hills should be less concentrated near the bottom than observed in the 21-22°S; 16-19°W region.

To account for this variability, we test a range of scenarios defined by $H_{bot} \propto A_{rms}^{l}$ and $r_{bot} \propto A_{rms}^{p}$, with $l \in \{-2, -1, -0.5, 0\}$ and $p \in \{-0.5, 0, 0.5, 1\}$. Combined to the values H_{bot} = 150 m and $r_{bot} = 0.86$ appropriate to the eastern Brazil Basin, the scenarios define global geographies of the two parameters. We then apply the complete parameterization to the WOCE annual mean climatology of stratification (Gouretski and Koltermann 2004) and compare the obtained distribution of $\epsilon_{tid} = \epsilon_{hil} + \epsilon_{cri} + \epsilon_{sho} + \epsilon_{wwi}$ to available microstructure observations across the globe (Fig. 7a; see section 3 for an expanded description). In particular, we sample the parameterized ϵ_{tid} along microstructure profiles and compare project-average profiles (Fig. 8). We find that $H_{bot} \propto A_{rms}^{-1}$ (Fig. 3b,c) and a constant r_{bot} generate the best overall agreement. Specifically, a steeper decrease of H_{bot} with A_{rms} or an increase of r_{bot} with A_{rms} promotes underestimation (overestimation) of the near-bottom dissipation in sampled regions where A_{rms} is relatively weak (strong). Zonal and vertical patterns of measured

[1] Scaling equation (7) in Lefauve et al. 2015 gives $A_{rms} \propto C(k_{hil})^{1/2} J(k_{hil}) k_{hil}^2$, where C is the 2-D spectrum for small-scale bathymetry, and J is the Bessel function of the first kind of order one. Scaling equation (7) in Polzin 2009, and omitting tidal harmonics, gives $E_{hil}(k_{hil}) \propto C(k_{hil}) J^2(k_{hil}) k_{hil}^{-1/2}$. Combining the two scalings gives $A_{rms} \propto E_{hil}^{1/2} k_{hil}^{3/2}$.

dissipation across the Brazil Basin provide the strongest constraint. The scenario $H_{bot} \propto A_{rms}^{-1}$ and r_{bot} = 0.86 gives a reasonable match between the parameterization and BBTRE across the basin and throughout the water column (Figs. 8 and 9). In the following, we retain this scenario exclusively and document the resultant climatological distribution of ϵ_{tid}.

3. Comparison to microstructure and finestructure observations

a. Microstructure

Our compilation of microstructure data (Fig. 7a) includes field campaigns described and analyzed by Waterhouse et al. (2014) as well as data from eight additional projects: INDOMIX (Bouruet-Aubertot et al. 2018a); OUTPACE (Bouruet-Aubertot et al. 2018b); three cruises over the Izu-Ogasawara ridge, hereafter referred to as IZU (Hibiya et al. 2012); DoMORE (Thurnherr et al. 2020); RidgeMix (Vic et al. 2018), OVIDE (Ferron et al. 2014), RREX (Petit et al. 2018) and PROVOLO (Fer et al. 2019). The compilation encompasses a total of 19 campaigns cumulating 1171 microstructure profiles. Only two profiles, from station 5 of the INDOMIX dataset, are excluded from the present analysis. Located in Ombai Strait, these profiles feature dissipation rates in excess of 10^{-4} W kg^{-1}, likely related to large internal solitary waves (Bouruet-Aubertot et al. 2018a), that overwhelm the regional average. Following Waterhouse et al. (2014), we split the BBTRE dataset into eastern (BBTREe: east of 28°W) and western (BBTREw: west of 28°W) regions (Fig. 7a). Measured viscous dissipation rates are binned into 200 m depth intervals and multiplied by $(1 - R_f)^{-1} = 6/5$ to obtain profiles of turbulence production. Project-average profiles are shown in black in Fig. 8.

Comparison with the parameterized ϵ_{tid} profiles (Fig. 8, blue) yields mixed results. Good agreement is found for NATRE, BBTREw, BBTREe, RidgeMix and DoMORE. Some overestimation of the deepest measurements from the latter three campaigns is nonetheless apparent. A reasonable match in magnitude but departures in shape are obtained for GEOTRACES, OVIDE, DIMES-DP, HOME, LADDER and INDOMIX. In several other cases, namely IZU, RREX, GRAVILUCK, OUTPACE and TOTO, the parameterization reproduces the shape but substantially overestimates the magnitude of the observational profile below 200 m. In the remaining SOFine, DIMES-West, PROVOLO and Fieberling areas, the parameterization predicts lower turbulence production than was measured.

Discrepancies can be explained by: (i) biases of the parameterization; (ii) non-tidal energy sources; (iii) application of the parameterization to a gridded annual mean stratification field, that may depart from the local stratification at the time of measurements; (iv) variability of turbulence that limits representativeness of measurements; and (v) measurement uncertainty. Substantial overestimates of turbulence production by the parameterization most likely stem from (i). Biased internal tide generation rates near Iceland (Lefauve et al. 2015) may contribute to RREX and OVIDE mismatches. A lack of energy redistribution in the model, possibly linked to overly strong attenuation by wave-wave interactions (de Lavergne et al. 2019), could also explain overestimates around generation sites such as IZU. Localized biases in mapped internal tide sources and sinks likely contribute to large magnitude offsets at TOTO, GRAVILUCK and Fieberling sites. Explanation (ii) is designated for the three Southern Ocean surveys (SOFine, DIMES-West and DIMES-DP): internal waves generated by atmospheric storms or jet-topography interactions likely dominate turbulence production in these areas (Ledwell et al. 2011, St Laurent et al. 2012, Waterman et al. 2013). In general, non-modelled processes are expected to contribute to salient mismatches in shape or amplitude.

Microstructure profilers provide instantaneous local measurements of patchy and intermittent turbulence, so that spatio-temporal variability and limited sampling will also account for some differences between observations and the ϵ_{tid} climatology. In particular, seasonal modulation of stratification, the spring-neap tidal cycle, and differences in seafloor depth between the 0.5°-resolution climatology and local observational casts can blur the comparison. For example, analysis of the timing of RREX observations along the Reykjanes ridge crest relative to the spring-neap cycle indicates that the measurements are biased toward neap tides on average (not shown). This sampling bias could contribute to the discrepancy with the parameterization. Microstructure-derived dissipations also have intrinsic uncertainty, thought to be about a factor of 2, attributable in part to sensor calibration and to the translation of microscale shear spectra into frictional dissipation rates (e.g., Toole et al. 1994). We note that a recent reinterpretation of the DoMORE raw data (see Appendix in Thurnherr et al. 2020) produces dissipation rates (used here) that are larger than those initially estimated (Clément et al. 2017), leading to better agreement with BBTRE and with the present parameterization.

Viewed overall, the comparison in Fig. 8 suggests that the parameterization captures reasonably well contrasts of turbulence production across regions and between ocean layers. For example, the gap of three orders of magnitude between Indonesian seas (INDOMIX) and the subtropical northeast Atlantic (NATRE) is correctly reproduced. The predicted vertical structure is also realistic in most cases; exceptions tend to coincide with regions for which there is evidence that internal tides are not the main conduit to small-scale turbulence. Hence, the constructed two-dimensional maps (Figs. 2 and 3) combined to chosen vertical structures (equations (2), (3), (5) and (7)) appear to have skill in mimicking turbulence powered by internal tides. This skill is exemplified by the Brazil Basin transect shown in Fig. 9 and further endorsed by the two-dimensional histogram of Fig. 10a. In spite of scatter in microstructure data and variability

across four orders of magnitude, turbulence levels and trends are generally comparable in the in-situ and climatological datasets. In particular, 85% of the 13,733 values in the microstructure database agree with ϵ_{tid} within a factor of 10; 41% of values agree within a factor of 2.

b. Finestructure

Internal wave energy dissipation can be estimated from the finescale strain contained in hydrographic casts (Polzin et al. 1995, Whalen et al. 2012). Such finestructure dissipation estimates carry large uncertainties because of choices and parameters involved in the inference (Polzin et al. 2014, Pollmann et al. 2017). Nonetheless, they allow extensive spatial coverage in comparison to microstructure measurements (Fig. 7). Here we analyse full-depth dissipation estimates of Kunze (2017) based on shipboard CTD casts (Fig. 7b), and upper-ocean dissipation estimates of Whalen et al. (2015) based on Argo CTD profiles (Fig. 7c). Values shallower than 380 m are considered unreliable by Kunze (2017) due to influence of the mixed layer on calculated strain. Whalen et al. (2015) exclude the mixed layer and mode water from the processing of individual Argo profiles. The Argo-based dataset employed here spans the 300-1900 m depth range and consists of average profiles binned into $1^\circ \times 1^\circ$ grid squares.

Comparison of finestructure observational estimates to the present climatology at 400 m depth reveals strong similarities (Fig. 11), consistent with previous findings (de Lavergne et al. 2019). The western low-latitude Pacific stands out as the most dissipative region, followed by western Indian and mid-Atlantic waters. The imprint of ridges hosting strong internal tide generation and dissipation is visible in all three maps, in spite of the relatively shallow depth (400 m) shown here. Enhanced dissipation above the Izu-Ogasawara ridge (which extends south of Japan) is conspicuous in the present (Fig. 11a) and Argo-finestructure (Fig. 11c) datasets, though less

intense in the latter. This local difference in magnitude reflects a more general tendency: basin-scale horizontal contrasts appear to be amplified in the ϵ_{tid} climatology relative to finestructure observations. Such a pattern amplification, previously identified in depth-integrated dissipation rates, could reflect an underestimation of energy redistribution in the two-dimensional mapping (de Lavergne et al. 2019).

Other regional discrepancies are apparent. Whalen et al. (2015) and Kunze (2017) infer larger internal wave energy loss near major currents such as the Kuroshio, Gulf Stream, Agulhas Current and Antarctic Circumpolar Current. These regions host intense mesoscale activity and above-average near-inertial energy input from atmospheric storms (e.g., Shum et al. 1990, Alford 2003). It is likely that non-tidal processes account for the bulk of the inferred internal wave energy dissipation there (Nikurashin et al. 2012, Waterman et al. 2014, Clément et al. 2016, Pollmann et al. 2017, Whalen et al. 2018), and therefore for the discrepancy with the present climatology. The dissipation map of Whalen et al. (2015) also displays a band of enhanced turbulence along the equator (Fig. 11c) that is absent from the ϵ_{tid} climatology (Fig. 11a). The elevated dissipation rates likely signal equatorial processes unrelated to internal tides, and possibly unrelated to inertio-gravity waves (e.g., Moum et al. 2009, Holmes and Thomas 2015). The inferred dissipation agrees with microstructure measurements at a western Pacific site (154-158°E) on the equator (Whalen et al. 2015). However, the equatorial band does not stand out in other finestructure estimates (Fig. 11b; Kunze 2017, Pollmann et al. 2017). A dedicated microstructure survey along the equator would be needed to establish whether this mixing pattern is real.

By sampling the parameterized ϵ_{tid} distribution along each finestructure profile, we can compare mean vertical profiles of turbulence production (Fig. 12). On average, turbulence production

has a very similar vertical distribution in the present and Argo-finestructure datasets (Fig. 12d-f). This agreement owes much to the scaling $\epsilon(z) \propto N^2(z)$, valid within most water columns of the open ocean in the 0.3 - 2 km depth range. This scaling is built in present and finestructure parameterizations, but also endorsed by microstructure data (Gregg 1989, Polzin et al. 1995). Fair agreement of ϵ_{tid} with the ship-based mean finestructure profile is also observed above 1.5 km depth (Fig. 12a-c). However, the mean ϵ_{tid} profile exceeds its finestructure counterpart by almost an order of magnitude deeper than 2 km (Fig. 12a). This excess is most pronounced in regions where abyssal hills and critical slopes are dominant contributors to internal tide dissipation (Fig. 12b). These regions are characterized by elevated deep-ocean turbulence production catalysed by rough or steep topography. A transect across the Atlantic near 23°S further illustrates the divide (Fig. 13): although the present parameterization and finestructure estimates compare well in the upper 2 km, finestructure-inferred dissipation is substantially weaker in the abyss. Indian and Pacific transects exhibit analogous similarities and differences (Supplementary Figs. S1 and S2).

The tidal dissipation climatology compares more favourably with deep microstructure data than with deep finestructure inferences (Figs. 8, 9, 12 and 13). Together with a comparison of neighbour finestructure and microstructure profiles (Supplementary Fig. S3), this suggests that finestructure estimates of Kunze (2017) are biased low in the deep ocean. In particular, the estimates seem to under-predict bottom-intensified dissipation above rough or steep topography. This assessment concurs with recent studies reporting underestimated dissipation by the employed finestructure method in regions of rough topography or strong forcing (Thurnherr et al. 2015, Bouruet-Aubertot et al. 2018a, Liang et al. 2018). The identified low bias is not expected to be universal, however, as it depends on implementation choices of the method and regional processes at play (Hibiya et al. 2012, Waterman et al. 2014, Takahashi and Hibiya

2018, Kunze and Lien 2019). We note that profiles of Fig. 12d-f also hint at a divergence near 1.7 km depth between the present parameterization and the dissipation estimates of Whalen et al. (2015).

In summary, the ϵ_{tid} climatology and finestructure observations display similar horizontal patterns and similar vertical structure in the upper ocean (Figs. 11-13 and Supplementary Figs. S1-S3). A histogram comparison of the global three-dimensional distributions (Fig. 10b-d) confirms the strong correlation between ϵ_{tid} and finestructure-inferred dissipation across five orders of magnitude. Agreement within a factor of 10 reaches 93% of values in the Argo-based dataset and 86% of values in the ship-based dataset. The latter percentage increases to 89% when excluding depths > 2 km. These results support the realism of the present tidal mixing parameterization and suggest that internal tides largely shape the global distribution of turbulence production.

4. Global distribution of internal tide-driven mixing

The parameterization proposed in this study allows visualization and quantification of the global distribution of turbulence production due to internal tides. The zonal sum of ϵ_{tid} shows that the bulk of turbulence production takes place in the upper kilometre of low and middle latitudes (Fig. 14a). This concentration is largely explained by the influence of stratification on internal tide generation and dissipation rates. In these strongly stratified waters, the parameterized mixing is mainly attributable to low-mode internal tides dissipating through wave-wave interactions (Fig. 14b) and to shoaling-induced wave breaking near continental margins (Fig. 14c). Critical slopes cause turbulence relatively evenly distributed in the upper 2.5 km (Fig. 14d), where most

steep continental slopes lie. Deeper than 2.5 km, tidal mixing mostly originates from internal tide generation and scattering by small-scale topographic roughness (Fig. 14e). The seafloor area distribution of ridges has a distinct footprint in the zonal sum of ϵ_{hil}, noticeable as a band of relatively high dissipation at abyssal depths (mostly between 2.5 and 4.5 km).

The distribution of the parameterized internal tide energy dissipation as a function of depth or height above bottom is presented in Figs. 15 and 16. The top kilometre of the ocean hosts 70% of the total energy loss (Fig. 16b), with contributions from all four components (Fig. 15a). This leaves only 311 GW, from the total of 1044 GW, of power input to small-scale turbulence at depths greater than 1 km. Between 1 and 2 km depth, energy loss amounts to 123 GW, fuelled mostly by modes ≤ 10 dissipating via wave-wave interactions and critical slopes. Below 2 km depth, power availability drops to 18% of the total and is dominated by the ϵ_{hil} component.

Almost 300 GW dissipate in the bottom 500 m of the ocean (Fig. 15b), including 180 GW in the open ocean (Fig. 15c). Components of dissipation linked to topography dwindle rapidly with height above bottom: $\epsilon_{hil} + \epsilon_{cri} + \epsilon_{sho}$ contributes little power at $h_{ab} > 2$ km. This trend is opposed by the large ϵ_{wwi} component, so that the overall power distribution decreases only gradually with h_{ab} beyond the bottom 500 m.

Hence, only about 30% of internal tide-induced energy dissipation occurs in the immediate vicinity of topography (Fig. 15b), and only about 300 GW contributes to mixing below 1 km depth (Fig. 15a). This budget contrasts with the notion put forth by Munk and Wunsch (1998) that internal tides supply about 1 TW of power to deep-ocean mixing, primarily along the bottom boundary. In reality, the bulk of the energy of internal tides contributes to mixing the upper ocean, away from topography. This finding highlights the efficient energy redistribu-

tion achieved by internal tides, and the concentration of vertical gradients in the upper ocean. Notwithstanding, the estimated power distribution does not necessarily imply a sluggish abyssal overturning nor 'missing mixing' in the deep ocean: sizeable overturning transports can be maintained below 2.5 km depth with moderate power input to mixing, owing to the weak stratification and large seafloor areas at these depths (de Lavergne et al. 2016, 2017).

We now compare the predicted distribution of internal tide energy loss to that implied by standard parameterizations of tidal mixing. In the NEMO model (version 3; Madec et al. 2016), one-third of the power input to internal tides mapped by Nycander (2005) is distributed in the local water column, using an exponential decay with h_{ab} and an e-folding scale of 500 m. A constant diffusivity of 10^{-5} m^2 s^{-1}, reduced to 10^{-6} m^2 s^{-1} near the equator, is added to represent so-called background mixing (Mignot et al. 2013). The CCSM model (version 4; Danabasoglu et al. 2012) follows an analogous approach but uses a distinct latitude-dependence of the background diffusivity (Jochum 2009) and the formulation of Jayne and St Laurent (2001) in place of the static map of Nycander (2005). For a meaningful comparison, the NEMO and CCSM parameterizations are applied here to the WOCE climatology (Gouretski and Koltermann 2004). Background diapycnal diffusivities K_ρ are converted into turbulence production rates ϵ using $R_f = 1/6$ and $\epsilon = R_f^{-1} K_\rho N^2$ (Osborn 1980).

The three parameterizations of tidal mixing produce depth distributions of turbulence production that differ in several ways (Fig. 16). The CCSM parameterization implies larger power input to mixing in the upper ocean, mostly due to relatively high background diffusivities (averaging 1.68×10^{-5} m^2 s^{-1} globally compared to 0.83×10^{-5} m^2 s^{-1} in the NEMO standard). The present parameterization produces the weakest power input at mid-depths (between 0.5 and 2.5 km), but the largest in the abyss (below 2.5 km). Three main factors underpin this shift of

energy toward the abyssal ocean: (i) the present parameterization accounts for variations in the modal distribution of internal tide generation, hence for the stronger local dissipation at abyssal sites relative to mid-depth sites (de Lavergne et al. 2019, Vic et al. 2019); (ii) low-mode internal tides have been tracked from sources (mostly at steep mid-depth topography) to sinks (mostly in shallow layers and above abyssal hills); (iii) the present scheme, unlike the other two, includes internal tide generation by abyssal hills. These effects focus the transition from $\mathcal{O}(10^{-5}\ \mathrm{m^2\ s^{-1}})$ to $\mathcal{O}(10^{-4}\ \mathrm{m^2\ s^{-1}})$ zonal mean diffusivities near 2.5 km depth (Fig. 17a,b).

More dramatic differences exist in the horizontal distribution of dissipation and mixing (Fig. 17c-f). The pronounced lateral heterogeneity of mixing rates mapped here contrasts with the more uniform diffusivities in the NEMO (or CCSM) standard parameterization. Mixing rates are strongly shaped by sources and sinks of internal tide energy, in the abyssal ocean (Fig. 17e) as well as in the pycnocline (Fig. 17c). The resultant complex patterns of mixing are not reproduced when remote tidal mixing is represented by a background diffusivity that varies only with latitude (Fig. 17d,f). Reduced diffusivities in the equatorial band (Gregg et al. 2003) are not found here: rather, a zonal gradient of diffusivity, between the eastern and western Pacific, is predicted (Fig. 17c) and corroborated by finestructure estimates of Kunze (2017) (Fig. 11b). The more realistic horizontal distribution of mixing produced by the present scheme may have important consequences for the simulated ocean and climate states (Zhu and Zhang 2019), including biogeochemical cycles (Tuerena et al. 2019).

5. Conclusions

Building upon a recent mapping of depth-integrated internal tide dissipation rates (de Lavergne

et al. 2019), we have proposed a comprehensive and energy-constrained parameterization of mixing powered by internal tides. This parameterization uses four static two-dimensional maps of available power (Fig. 2), each associated with a specific dissipative pathway and a relevant vertical structure of turbulence production (equations (2), (3), (5) and (7)). The scheme explicitly accounts for the near-field dissipation of small-scale internal tides and the far-field dissipation of larger scale internal tides, without assuming a constant proportion of near-field dissipation. Vertical structures incorporate three parameters (H_{cri}, H_{bot} and r_{bot}) which have been calibrated and mapped (Fig. 3) with the aid of previous observational and theoretical studies (Polzin et al. 1997, Legg and Adcroft 2003, Polzin 2009, Lefauve et al. 2015).

The proposed parameterization has been applied to an observational climatology of stratification to obtain a global three-dimensional map of turbulence production. Comparison of this map to a compilation of observational mixing estimates shows that the parameterization has skill in reproducing horizontal and vertical patterns of mixing. The comparison also suggests that, in the ocean interior, internal tides are the principal energy source for mixing and are responsible for the main large-scale patterns of mixing. This inference is consistent with the large power input to internal tides (~ 1 TW) and with the relative temporal stability of basin-scale dissipation patterns (Ferron et al. 2016, Kunze 2017). The estimated climatology of internal tide energy loss further shows that 70% of the total power lies in the upper kilometre of the ocean. Hence, internal tides contribute first and foremost to mix the upper ocean—in spite of their generation at the bottom boundary.

The parameterization can also be applied to model oceans. Its implementation in OGCMs merely necessitates a remapping of static maps (Figs. 2 and 3) onto the model grid, and distribution of turbulence production in the vertical according to the simulated stratification. While

the available power within each water column is fixed in time, the vertical structure of the energy supply thus evolves with the simulated density profile. Experiments performed with the NEMO model (which will be documented elsewhere) showed that the parameterization obviates the need for a constant background diffusivity above molecular levels, and therefore ensures that explicit diapycnal mixing in the model is energy-constrained. This essential property, together with the scheme's low computational cost, motivated its implementation in several climate models participating to phase 6 of the Coupled Model Intercomparison Project (cf. Voldoire et al. 2019).

Naturally, the use of static maps representative of modern mean ocean conditions disallows representation of transient changes in the horizontal distribution of internal tide energy loss, and limits applicability to other climate states. Nonetheless, we expect only weak sensitivity of this horizontal distribution to climate-driven changes in ocean stratification (Egbert et al. 2004). This expectation is backed by an experiment in which we perturbed the climatological stratification entering the two-dimensional mapping procedure. Specifically, we calculated the change in buoyancy frequency between periods 1860-1910 and 2100-2150 of a HadGEM2-ES simulation (Collins et al. 2011) forced by historical and RCP8.5 boundary conditions, and multiplied the WOCE climatological buoyancy frequency by this change (expressed as the ratio of the later to the earlier period, in $h_{wkb,1}$ vertical coordinate). Despite the high climate sensitivity of HadGEM2-ES (Andrews et al. 2012), this perturbation led to marginal changes in the geography of internal tide energy sinks (Table 2). By contrast, the total energy consumption implied by a constant diapycnal diffusivity K_ρ, calculated as $\iiint R_f^{-1} K_\rho N^2 dM$ with dM the unit mass, increases by 40% between the two periods. Hence, imposing a constant diffusivity can lead to large, spurious and uncontrolled changes in the magnitude and distribution of turbulence production. This prejudicial behaviour, and its potential consequences for model drift and

simulated climate (Eden et al. 2014), are avoided by the proposed mixing parameterization.

In spite of its advantages, the parameterization leaves substantial room for improvement. First, its realism is limited by approximations and simplifications of the two-dimensional mapping procedure, and notably by the ad hoc representation of internal tide attenuation by wave-wave interactions (de Lavergne et al. 2019). Interactions with balanced flows and with low-mode near-inertial waves have not been modelled despite evidence for impacts on propagation and dissipation (Rainville and Pinkel 2006, Ponte and Klein 2015, Cuypers et al. 2017). More accurate and comprehensive internal tide generation estimates, accounting for all bathymetric scales and slopes, would also improve the fidelity of the parameterization. Sub-annual variability, including seasonal and spring-neap variations of internal tide generation and dissipation, has been ignored in the construction of static maps: its impact deserves further investigation. Second, vertical structures also incorporate important simplifications and uncertainties. For example, the calibration of r_{bot} and H_{bot} parameters did not account for the varying efficiency of triadic wave instabilities (Nikurashin and Legg 2011, Richet et al. 2017) nor for the effects of internal lee waves (Hibiya et al. 2017). Further work is needed to better constrain these two parameters, and thereby to alleviate biases in the predicted mixing above ridge flanks. Refinement of the vertical structure (2), to account for various scenarios of local or remote dissipation via wave-wave interactions, should also be pursued. Third, the present parameterization only represents mixing powered by propagating internal tides. Other tidal contributions to mixing, namely bottom-trapped internal tides (e.g., Müller 2013, Falahat and Nycander 2014) and frictional drag of barotropic tides (e.g., Lee et al. 2006), have not been considered. These contributions could be added provided suitable maps of available power can be obtained.

The degree of agreement between the parameterized distribution of internal tide-driven mixing

and observational estimates of mixing (Figs. 8-12) indicates that the parameterization can serve a range of purposes, including forward and inverse modelling, water-mass transformation estimates, regional to global tracer budgets, and context for field campaigns. Conversely, new field campaigns and numerical studies will help to narrow down uncertainties, expose biases, and identify avenues for improvement of the modelled distribution of turbulence production.

Acknowledgements

We thank all investigators involved in the collection of microstructure measurements analysed here. Efforts to gather and publish historical microstructure datasets (see https://microstructure.ucsd.edu) are also gratefully acknowledged. We thank E. Kunze, I. Fer, L. Clément, A. Melet and J. Goff for sharing their published datasets. J. Nycander and L. Clément provided helpful comments on the manuscript. Static maps entering the present parameterization and three-dimensional fields computed using the WOCE hydrographic climatology are made available at: *link to be provided before publication*. This project has received funding from the European Union's Horizon 2020 research and innovation programme under grant agreement N°821001.

References

Alford, M.H., 2003. Improved global maps and 54-year history of wind-work on ocean inertial motions. *Geophys. Res. Lett.* **30**, 1424.

Andrews, T., Gregory, J.M., Webb, M.J., Taylor, K.E., 2012. Forcing, feedbacks and climate sensitivity in CMIP5 coupled atmosphere-ocean climate models. *Geophys. Res. Lett.* **39**,

L09712.

Bell, T.H., 1975. Topographically generated internal waves in the open ocean. *J. Geophys. Res.* **80**, 320-327.

Bouruet-Aubertot, P., Cuypers, Y., Ferron, B., Dausse, D., Ménage, O., Atmadipoera, A., Jaya, I., 2018a. Contrasted turbulence intensities in the Indonesian Throughflow: a challenge for parameterizing energy dissipation rate. *Ocean Dynamics* **68**, 779-800.

Bouruet-Aubertot, P., Cuypers, Y., Doglioli, A., Caffin, M., Yohia, C., de Verneil, A., Petrenko, A., Lefèvre, D., Le Goff, H., Rougier, G., Picheral, M., Moutin, T., 2018b. Longitudinal contrast in turbulence along a $\sim 19°$S section in the Pacific and its consequences for biogeochemical fluxes. *Biogeosciences* **15**, 7485-7504.

Bühler, O., Holmes-Cerfon, M., 2011. Decay of an internal tide due to random topography in the ocean. *J. Fluid Mech.* **678**, 271-293.

Clément, L., Frajka-Williams, E., Sheen, K.L., Brearley, J.A., Naveira Garabato, A.C., 2016. Generation of internal waves by eddies impinging on the western boundary of the North Atlantic. *J. Phys. Oceanogr.* **46**, 1067-1079.

Clément, L., Thurnherr, A., St Laurent, L.C., 2017. Turbulent mixing in a deep fracture zone on the Mid-Atlantic Ridge. *J. Phys. Oceanogr.* **47**, 1873-1896.

Cuypers, Y., Bouruet-Aubertot, P., Vialard, J., McPhaden, M.J., 2017. Focusing of internal tides by near-inertial waves. *Geophys. Res. Lett.* **44**, 2398-2406.

Collins, W.J., Bellouin, N., Doutriaux-Boucher, M., Gedney, N., Halloran, P., Hinton, T., Hughes, J., Jones, C.D., Joshi, M., Liddcoat, S., Martin, G., O'Connor, F., Rae, J., Senior, C., Sitch, S., Totterdell, I., Wiltshire, A., Woodward, S., 2011. Development and evaluation of an Earth-System model – HadGEM2. *Geosci. Model Dev.* **4**, 1051-1075.

D'Asaro, E.A., Lien, R.-C., 2000. The wave–turbulence transition for stratified flows. *J. Phys. Oceanogr.* **30**, 1669-1678.

593 de Lavergne, C., Madec, G., Le Sommer, J., Nurser, A.J.G., Naveira Garabato, A.C., 2016. On
594 the consumption of Antarctic Bottom Water in the abyssal ocean. *J. Phys. Oceanogr.* **46**,
595 635-661.
596 de Lavergne, C., Madec, G., Roquet, F., Holmes, R.M., McDougall, T.J., 2017. Abyssal ocean
597 overturning shaped by seafloor distribution. *Nature* **551**, 181-186.
598 de Lavergne, C., Falahat, S., Madec, G., Roquet, F., Nycander, J., Vic, C., 2019. Toward global
599 maps of internal tide energy sinks. *Ocean Modelling* **137**, 52-75.
600 Danabasoglu, G., Bates, S.C., Briegleb, B.P., Jayne, S.R., Jochum, M., Large, W.G., Peacock,
601 S., Yeager, S.G.,2012. The CCSM4 ocean component. *J. Clim.* **25**, 1361-1389.
602 Dushaw, B.D., Cornuelle, B.D., Worcester, P., Howe, B.M., Luther, D.S., 1995. Barotropic
603 and baroclinic tides in the central North Pacific ocean determined from long-range reciprocal
604 acoustic transmissions. *J. Phys. Oceanogr.* **25**, 631-647.
605 Eden, C., Olbers, D., 2014. An energy compartment model for propagation, nonlinear interac-
606 tion, and dissipation of internal gravity waves. *J. Phys. Oceanogr.* **44**, 2093-2106.
607 Eden, C., Czeschel, L., Olbers, D., 2014. Towards energetically consistent ocean models. *J.*
608 *Phys. Oceanogr.* **44**, 3160-3184.
609 Egbert, G.D., Ray, R.D., Bills, B.G., 2004. Numerical modelling of the global semidiurnal tide
610 in the present day and in the last glacial maximum. *J. Geophys. Res.* **109**, C03003.
611 Eriksen, C.C., 1982. Observations of internal wave reflection off sloping bottoms. *J. Geophys.*
612 *Res.* **87**, 525-538.
613 Falahat, S., Nycander, J., Roquet, F., Thurnherr, A.M., Hibiya, T., 2014a. Comparison of cal-
614 culated energy flux of internal tides with microstructure measurements. *Tellus A* **66**, 23240.
615 Falahat, S., Nycander, J., Roquet, F., Moundheur, Z., 2014b. Global calculation of tidal energy
616 conversion into vertical normal modes. *J. Phys. Oceanogr.* **44**, 3225-3244.
617 Falahat, S., Nycander, J., 2014. On the generation of bottom-trapped internal tides. *J. Phys.*

618 *Oceanogr.* **45**, 526-545.

619 Fer, I., Bosse, A., Soiland, H., Ferron, B., Bouruet-Aubertot, P., 2019. Ocean currents, hydrog-
620 raphy and microstructure data from PROVOLO cruises. https://doi.org/10.21335/NMDC-
621 1093031037

622 Ferron, B., Kokoszka, F., Mercier, H., Lherminier, P., 2014. Dissipation rate estimates from
623 microstructure and finescale internal wave observations along the A25 Greenland-Portugal
624 OVIDE line. *J. Atmos. Oceanic Technol.* **31**, 2530-2543.

625 Ferron, B., Kokoszka, F., Mercier, H., Lherminier, P., Huck, T., Rios, A., Thierry, V., 2016.
626 Variability of the turbulent kinetic energy dissipation along the A25 Greenland-Portugal tran-
627 sect repeated from 2002 to 2012. *J. Phys. Oceanogr.* **46**, 1989-2003.

628 Goff, J.A., 2010. Global prediction of abyssal hill root-mean-square heights from small-scale
629 altimetric gravity variability. *J. Geophys. Res.* **115**, B12104.

630 Gouretski, V.V., Koltermann, K.P., 2004. WOCE global hydrographic climatology: a technical
631 report. Berichte des Bundesamtes für Seeschifffahrt und Hydrographie 35/2004, 52 pp.

632 Gregg, M.C., 1989. Scaling turbulent dissipation in the thermocline. *J. Geophys. Res.* **94**,
633 9686-9698.

634 Gregg, M.C., Sanford, T.B., Winkel, D.P., 2003. Reduced mixing from the breaking of internal
635 waves in equatorial waters. *Nature* **422**, 513-515.

636 Gregg, M.C., D'Asaro, E.A., Riley, J.J., Kunze, E., 2018. Mixing efficiency in the ocean. *Annu.*
637 *Rev. Mar. Sci.* **10**, 443-473.

638 Hazewinkel, J., Winters, K.B., 2011. PSI of the internal tide on a β plane: flux divergence and
639 near-inertial wave propagation. *J. Phys. Oceanogr.* **41**, 1673-1682.

640 Hibiya, T., Nagasawa, M., 2004. Latitudinal dependence of diapycnal diffusivity in the thermo-
641 cline estimated using a finescale parameterization. *Geophys. Res. Lett.* **31**, L01301.

642 Hibiya, T., Furuichi, N., Robertson, R., 2012. Assessment of fine-scale parameterizations of

turbulent dissipation near mixing hotspots in the deep ocean. *Geophys. Res. Lett.* **39**, L24601.

Hibiya, T., Ijichi, T., Robertson, R., 2017. The impacts of ocean bottom roughness and tidal flow amplitude on abyssal mixing. *J. Geophys. Res.* **122**, 5645-5651.

Holmes, R.M., Thomas, L.N., 2015. The modulation of equatorial turbulence by tropical instability waves in a regional ocean model. *J. Phys. Oceanogr.* **45**, 1155-1173.

Jayne, S.R., St Laurent, L.C., 2001. Parameterizing tidal dissipation over rough topography. *Geophys. Res. Lett.* **28**, 811-814.

Jochum, M., 2009. Impact of latitudinal variations in vertical diffusivity on climate simulations. *J. Geophys. Res.* **114**, C01010.

Kunze, E., Firing, E., Hummon, J.M., Chereskin, T.K., Thurnherr, A.M., 2006. Global abyssal mixing inferred from lowered ADCP shear and CTD strain profiles.. *J. Phys. Oceanogr.* **36**, 1553-1576.

Kunze, E., 2017. Internal wave-driven mixing: global geography and budgets. *J. Phys. Oceanogr.* **47**, 1325-1345.

Kunze, E., Lien, R.-C., 2019. Energy sinks for lee waves in shear flow. *J. Phys. Oceanogr.*, in press. https://doi.org/10.1175/JPO-D-19-0052.1.

Ledwell, J.R., Montgomery, E.T., Polzin, K.L., St Laurent, L.C., Schmitt, R.W., Toole, J.M., 2000. Evidence for enhanced mixing over rough topography in the abyssal ocean. *Nature* **403**, 179-182.

Ledwell, J.R., St Laurent, L.C., Girton, J.B., Toole, J.M., 2011. Diapycnal mixing in the Antarctic Circumpolar Current. *J. Phys. Oceanogr.* **41**, 241-246.

Lee, H.-C., Rosati, A., Spelman, M.J., 2006. Barotropic tidal mixing effects in a coupled climate model: Oceanic conditions in the northern Atlantic. *Ocean Modelling* **11**, 464-477.

Lefauve, A., Muller, C., Melet, A., 2015. A three-dimensional map of tidal dissipation over

668 abyssal hills. *J. Geophys. Res.* **120**, 4760-4777.

669 Legg, S., Adcroft, A., 2003. Internal wave breaking at concave and convex continental slopes.
670 *J. Phys. Oceanogr.* **33**, 2224-2246.

671 Legg, S., 2014. Scattering of low-mode internal waves at finite isolated topography. *J. Phys.*
672 *Oceanogr.* **44**, 359-383.

673 Liang, C.-R., Shang, X.-D., Qi, Y.-F., Chen, G.-Y., Yu, L.-H., 2018. Assessment of fine-scale
674 parameterizations at low latitudes of the North Pacific. *Scientific Reports* **8**, 10281.

675 Locarnini, R.A., Mishonov, A.V., Baranova, O.K., Boyer, T.P., Zweng, M.M., Garcia, H.E.,
676 Reagan, J.R., Seidov, D., Weathers, K., Paver, C.R., Smolyar, I., 2018. World Ocean Atlas
677 2018, Volume 1: Temperature. A. Mishonov Technical Ed.; NOAA Atlas NESDIS 81, 52 pp.

678 Macdonald, K.C., Fox, P.J., Alexander, R.T., Pockalny, R., Gente, P., 1996. Volcanic growth
679 faults and the origin of Pacific abyssal hills. *Nature* **380**, 125-129.

680 MacKinnon, J.A., Alford, M.H., Pinkel, R., Klymak, J., Zhao, Z., 2013a. The latitudinal de-
681 pendence of shear and mixing in the Pacific transiting the critical latitude for PSI. *J. Phys.*
682 *Oceanogr.* **43**, 3-16.

683 MacKinnon, J.A., Zhao, Z., Whalen, C.B., Waterhouse, A.F., Trossman, D.S., Sun, O.M., St
684 Laurent, L.C., Simmons, H.L., Polzin, K., Pinkel, R., Pickering, A., Norton, N.J., Nash, J.D.,
685 Musgrave, R., Merchant, L.M., Melet, A.V., Mater, B., Legg, S., Large, W.G., Kunze, E.,
686 Klymak, J.M., Jochum, M., Jayne, S.R., Hallberg, R.W., Griffies, S.M., Diggs, S., Danaba-
687 soglu, G., Chassignet, E.P., Buijsman, M.C., Bryan, F.O., Briegleb, B.P., Barna, A., Arbic,
688 B.K., Ansong, J.K., Alford, M.H., 2017. Climate process team on internal wave-driven ocean
689 mixing. *Bull. Am. Meteorol. Soc.* **98**, 2429-2454.

690 Madec, G., and the NEMO team, 2016. NEMO ocean engine. Scientific notes of climate
691 modelling center, **27** – ISSN 1288-1619, Insitut Pierre-Simon Laplace (IPSL).

692 Melet, A., Nikurashin, M., Muller, C., Falahat, S., Nycander, J., Timko, P.G., Arbic, B.K., Goff,

693 J.A., 2013a. Internal tide generation by abyssal hills using analytical theory. *J. Geophys. Res.*
694 **118**, 6303-6318.
695 Melet, A., Hallberg, R., Legg, S., Polzin, K., 2013b. Sensitivity of the ocean state to the vertical
696 distribution of internal-tide-driven mixing. *J. Phys. Oceanogr.* **43**, 602-615.
697 Melet, A., Legg, S., Hallberg, R., 2016. Climatic impacts of parameterized local and remote
698 tidal mixing. *J. Clim.* **29**, 3473-3500.
699 Mignot, J., Swingedouw, D., Deshayes, J., Marti, O., Talandier, C., Séférian, R., Lengaigne,
700 M., Madec, G., 2013. On the evolution of the oceanic component of the IPSL climate models
701 from CMIP3 to CMIP5: a mean state comparison. *Ocean Modell.* **72**, 167-184.
702 Moum, J.N., Caldwell, D.R., Nash, J.D., Gunderson, G.D., 2002. Observations of boundary
703 mixing over the continental slope. *J. Phys. Oceanogr.* **32**, 2113-2130.
704 Moum, J.N., Lien, R.-C., Perlin, A., Nash, J.D., Gregg, M.C., Wiles, P.J., 2009. Sea surface
705 cooling at the Equator by subsurface mixing in tropical instability waves. *Nat. Geosci.* **2**,
706 761-765.
707 Muller, C.J., Bühler, O., 2009. Saturation of the internal tides and induced mixing in the abyssal
708 ocean. *J. Phys. Oceanogr.* **39**, 2077-2096.
709 Müller, M., 2013. On the space- and time-dependence of barotropic-to-baroclinic tidal energy
710 conversion. *Ocean Modelling* **72**, 242-252.
711 Müller, P., Holloway, G., Henyey, F., Pomphrey, N., 1986. Nonlinear interactions among inter-
712 nal gravity waves. *Rev. Geophys.* **24**, 493-536.
713 Munk, W.H., 1966. Abyssal Recipes. *Deep Sea Res.* **13**, 707-730.
714 Munk, W., Wunsch, C., 1998. Abyssal recipes II: energetics of tidal and wind mixing. *Deep-Sea*
715 *Res.* **45**, 1977-2000.
716 Nash, J.D., Kunze, E., Toole, J.M., Schmitt, R.W., 2004. Internal tide reflection and turbulent
717 mixing on the continental slope. *J. Phys. Oceanogr.* **34**, 1117-1134.

718 Nikurashin, M., Legg, S., 2011. A mechanism for local dissipation of internal tides generated
719 at rough topography. *J. Phys. Oceanogr* **41**, 378-395.
720 Nikurashin, M., Vallis, G.K., Adcroft, A., 2012. Routes to energy dissipation for geostrophic
721 flows in the Southern Ocean. *Nat. Geosci.* **6**, 48-51.
722 Niwa, Y., Hibiya, T., 2011. Estimation of baroclinic tide energy available for deep ocean mixing
723 based on three-dimensional global numerical simulations. *J. Oceanogr.* **67**, 493-502.
724 Nycander, J., 2005. Generation of internal waves in the deep ocean by tides. *J. Geophys. Res.*
725 **110**, C10028.
726 Oka, A., Niwa, Y., 2013. Pacific deep circulation and ventilation controlled by tidal mixing
727 away from the sea bottom. *Nat. Comm.* **4**, 1-8.
728 Olbers, D.J., 1976. Nonlinear energy transfer and the energy balance of the internal wave field
729 in the deep ocean. *J. Fluid. Mech.* **74**, 375-399.
730 Olbers, D.J., 1983. Models of the oceanic internal wave field. *Rev. Geophys.* **21**, 1567-1606.
731 Osborn, T.R., 1980. Estimates of the local rate of vertical diffusion from dissipation measure-
732 ments. *J. Phys. Oceanogr.* **10**, 83-89.
733 Petit, T., Mercier, H., Thierry, V., 2018. First direct estimates of volume and water mass trans-
734 ports across the Reykjanes ridge. *J. Geophys. Res.* **123**, 6703-6719.
735 Pollmann, F., Eden, C., Olbers, D., 2017. Evaluating the global internal wave model IDEMIX
736 using finestructure methods. *J. Phys. Oceanogr.* **47**, 2267-2289.
737 Polzin, K.L., Toole, J.M., Schmitt, W., 1995. Finescale parameterizations of turbulent dissipa-
738 tion. *J. Phys. Oceanogr.* **25**, 306-328.
739 Polzin, K.L., Toole, J.M., Ledwell, J.R., Schmitt, W., 1997. Spatial variability of turbulent
740 mixing in the abyssal ocean. *Science* **276**, 93-96.
741 Polzin, K.L., 2004. Idealized solutions for the energy balance of the finescale internal wave
742 field. *J. Phys. Oceanogr.* **34**, 231-248.

743 Polzin, K.L., 2009. An abyssal recipe. *Ocean Modelling* **30**, 298-309.

744 Polzin, K.L., Naveira Garabato, A.C., Huussen, T.N., Sloyan, B.M., Waterman, S., 2014.
745 Finescale parameterizations of turbulent dissipation. *J. Geophys. Res.* **119**, 1383-1419.

746 Ponte, A.L., Klein, P., 2015. Incoherent signature of internal tides on sea level in idealized
747 numerical simulations. *Geophys. Res. Lett.* **42**, 1520-1526.

748 Rainville, L., Pinkel, R., 2006. Propagation of low-mode internal waves through the ocean. *J.*
749 *Phys. Oceanogr.* **36**, 1220-1236.

750 Ray, R.D., Mitchum, G.T., 1996. Surface manifestation of internal tides generated near Hawaii.
751 *Geophys. Res. Lett.* **23**, 2101-2104.

752 Richet, O., Muller, C., Chomaz, J.-M., 2017. Impact of a mean current on the internal tide
753 energy dissipation at the critical latitude. *J. Phys. Oceanogr.* **47**, 1457-1472.

754 Shum, C.K., Werner, R.A., Sandwell, D.T., Zhang, B.H., Nerem, R.S., Tapley, B.D., 1990.
755 Variations of global mesoscale eddy energy observed from Geosat. *J. Geophys. Res.* **95**,
756 17865-17876.

757 Sigman, D.M., Hain, M.P., Haug, G.H., 2010. The polar ocean and glacial cycles in atmospheric
758 CO2 concentration. *Nature* **466**, 47-55.

759 Simmons, H.L., Jayne, S.R., St Laurent, L.C., Weaver, A.J., 2004. Tidally driven mixing in a
760 numerical model of the ocean general circulation. *Ocean Modell.* **6**, 245-263.

761 Smith, W.H.F., Sandwell, D.T., 1997. Global sea floor topography from satellite altimetry and
762 ship depth soundings. *Science* **277**, 1956-1962.

763 St Laurent, L.C., Simmons, H.L., Jayne, S.R., 2002. Estimating tidally driven mixing in the
764 deep ocean. *Geophys. Res. Lett.* **29**, 2106.

765 St Laurent, L.C., Garrett, C., 2002. The role of internal tides in mixing the deep ocean. *J. Phys.*
766 *Oceanogr.* **32**, 2882-2899.

767 St Laurent, L.C., Nash, J.D., 2004. An examination of the radiative and dissipative properties

of deep ocean internal tides. *Deep-Sea Res.* **51**, 3029-3042.

St Laurent, L.C., Naveira Garabato, A.C., Ledwell, J.R., Thurnherr, A.M., Toole, J.M., Watson, A.J., 2012. Turbulence and diapycnal mixing in Drake Passage. *J. Phys. Oceanogr.* **42**, 2143-2152.

Takahashi, A., Hibiya, T., 2019. Assessment of finescale parameterizations of deep ocean mixing in the presence of geostrophic current shear: results of microstructure measurements in the Antarctic Circumpolar Current region. *J. Geophys. Res.* **124**, 135-153.

Thurnherr, A.M., Kunze, E., Toole, J..M., St Laurent, L., Richards, K.J., Ruiz-Angulo, A., 2015. Vertical kinetic energy and turbulent dissipation in the ocean. *Geophys. Res. Lett.* **42**, 7639-7647.

Thurnherr, A.M., Clément, L., St Laurent, L., Ferrari, R., Ijichi, T., 2020. Transformation and upwelling of bottom water in fracture zone valleys. *J. Phys. Oceanogr.*, in press. doi:10.1175/JPO-D-19-0021.1

Toole, J.M., Schmitt, R.W., Polzin, K.L., 1994. Estimates of diapycnal mixing in the abyssal ocean. *Science* **264**, 1120-1123.

Tuerena, R.E., Williams, R.G., Mahaffey, C., Vic, C., Green, J.A.M., Naveira Garabato, A., Forryan, A., Sharples, J., 2019. Internal tides drive nutrient fluxes into the deep chlorophyll maximum over mid-ocean ridges. *Global Biogeochem. Cycles* **33**, 995-1009.

Vic, C., Naveira Garabato, A.C., Green, J.A.M., Spingys, C., Forryan, A., Zhao, Z., Sharples, J., 2018. The lifecycle of semidiurnal tides over the northern Mid-Atlantic Ridge. *J. Phys. Oceanogr.* **48**, 61-80.

Vic, C., Naveira Garabato, A.C., Green, J.A.M., Waterhouse, A.F., Zhao, Z., Melet, A., de Lavergne, C., Buijsman, M.C., Stephenson, G.R., 2019. Deep-ocean mixing driven by small-scale internal tides. *Nat. Comm.* **10**, 2099.

Voldoire, A., Saint-Martin, D., Sénési, S., Decharme, B., Alias, A., Chevallier, M., Colin, J.,

Guérémy, J.-F., Michou, M., Moine, M.-P., Nabat, P., Roehrig, R., Salas y Mélia, D., Séférian, R., Valcke, S., Beau, I., Belamari, S., Berthet, S., Cassou, C., Cattiaux, J., Deshayes, J., Douville, H., Ethé, C., Franchistéguy, L., Geoffroy, O., Lévy, C., Madec, G., Meurdesoif, Y., Msadek, R., Ribes, A., Sanchez-Gomez, E., Terray, L., Waldman, R., 2019. Evaluation of CMIP6 DECK experiments with CNRM-CM6-1. *J. Adv. Modell. Earth Systems* **11**, 2177-2213.

Waterhouse, A.F., MacKinnon, J.A., Nash, J.D., Alford, M.H., Kunze, E., Simmons, H.L., Polzin, K.L., St Laurent, L.C., Sun, O.M., Pinkel, R., Talley, L.D., Whalen, C.B., Huussen, T.N., Carter, G.S., Fer, I., Waterman, S., Naveira Garabato, A.C., Sandord, T.B., Lee, C.M., 2014. Global patterns of diapycnal mixing from measurements of the turbulent dissipation rate. *J. Phys. Oceanogr.* **44**, 1854-1872.

Waterman, S., Naveira Garabato, A.C., Polzin, K.L., 2013. Internal waves and turbulence in the Antarctic Circumpolar Current. *J. Phys. Oceanogr.* **43**, 259-282.

Waterman, S., Polzin, K.L., Naveira Garabato, A.C., Sheen, K.L., Forryan, A., 2014. Suppression of internal wave breaking in the Antarctic Circumpolar Current near topography. *J. Phys. Oceanogr.* **44**, 1466-1492.

Whalen, C.B., Talley, L.D., MacKinnon, J.A., 2012. Spatial and temporal variability of global ocean mixing inferred from Argo profiles. *Geophys. Res. Lett.* **39**, L18612.

Whalen, C.B., MacKinnon, J.A., Talley, L.D., Waterhouse, A.F., 2015. Estimating the mean diapycnal mixing using a finescale strain parameterization. *J. Phys. Oceanogr.* **45**, 1174-1188.

Whalen, C.B., MacKinnon, J.A., Talley, L.D., 2018. Large-scale impacts of the mesoscale environment on mixing from wind-driven internal waves. *Nat. Geosci.* **11**, 842-847.

Zhu, Y., Zhang, R.-H., 2019. A modified vertical mixing parameterization for its improved ocean and coupled simulations in the tropical Pacific. *J. Phys. Oceanogr.* **49**, 21-37.

Zweng, M. M., Reagan, J.R., Seidov, D., Boyer, T.P., Locarnini, R.A., Garcia, H.E., Mishonov, A.V., Baranova, O.K., Weathers, K., Paver, C.R., Smolyar, I., 2018. World Ocean Atlas 2018, Volume 2: Salinity. A. Mishonov Technical Ed.; NOAA Atlas NESDIS 82, 50 pp.

Depth range [m]	Obs. composite [%]	Equation (7) (r_{bot}=0.86, H_{bot}=150m) [%]	Lefauve et al. 2015 (H_L=400m) [%]	Melet et al. 2013b (H_M=5m) [%]
0-750	33.1	34.1	29.3	34.6
750-1500	8.0	7.0	10.4	7.8
1500-2250	3.7	2.7	5.8	2.4
2250-3000	2.2	2.3	3.5	0.9
3000-3750	4.9	5.5	17.9	3.4
3750-4500	48.1	48.4	33.1	51.0

Table 1: Vertical distribution of power in the composite observational profile (21-22°S; 16-19°W) and three different parameterizations. The distribution is described by the percentage power contained in each 750 m-thick layer. All three parameterizations include $\epsilon_{hil} + \epsilon_{wwi}$. Only the vertical structure of ϵ_{hil} changes according to parameterization. The present parameterization of ϵ_{hil} uses r_{bot} = 0.86 and H_{bot} = 150 m. The structure proposed by Lefauve et al. (2015) is applied with H_L = 400 m; that proposed by Melet et al. (2013b) is applied with H_M = 5 m.

Constituent Experiment	M_2 REF	M_2 WARM
Power in modes 1-5 (GW)	564	564
Shelves (%)	4.8	4.9
Wave-wave interactions (%)	61.5	60.2
Scattering by hills (%)	9.9	10.7
Critical slopes (%)	14.9	14.9
Shoaling (%)	8.9	9.2

Table 2: Process contributions to M_2 low-mode internal tide dissipation in REF and WARM experiments. The REF experiment is the reference calculation documented in de Lavergne et al. (2019). The WARM experiment is identical to REF except for perturbed stratification as described in section 5. Shelves, defined as areas where the seafloor depth < 400 m, have been separated out in the decomposition by process. Only modes 1 to 5 of the M_2 tidal constituent are included in the total power and percentages given. The impact of the stratification change on the criticality/supercriticality of topographic slopes has been taken into account.

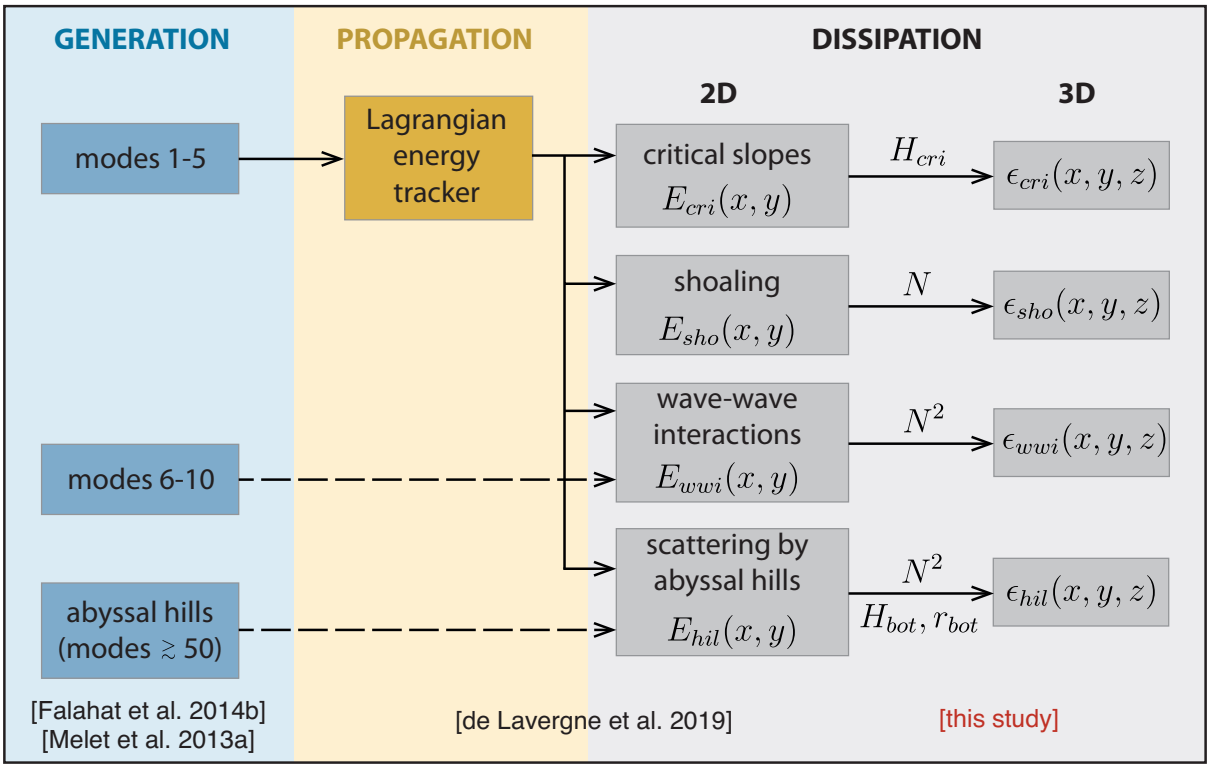

Figure 1: Diagram summarizing the approach. This study extends the dissipation maps from 2D to 3D by applying a vertical structure appropriate to each process-specific map of column-integrated internal tide energy loss. The vertical structures involve the buoyancy frequency N as well as parameters (H_{cri}, H_{bot}, r_{bot}) determined by comparison to microstructure observations.

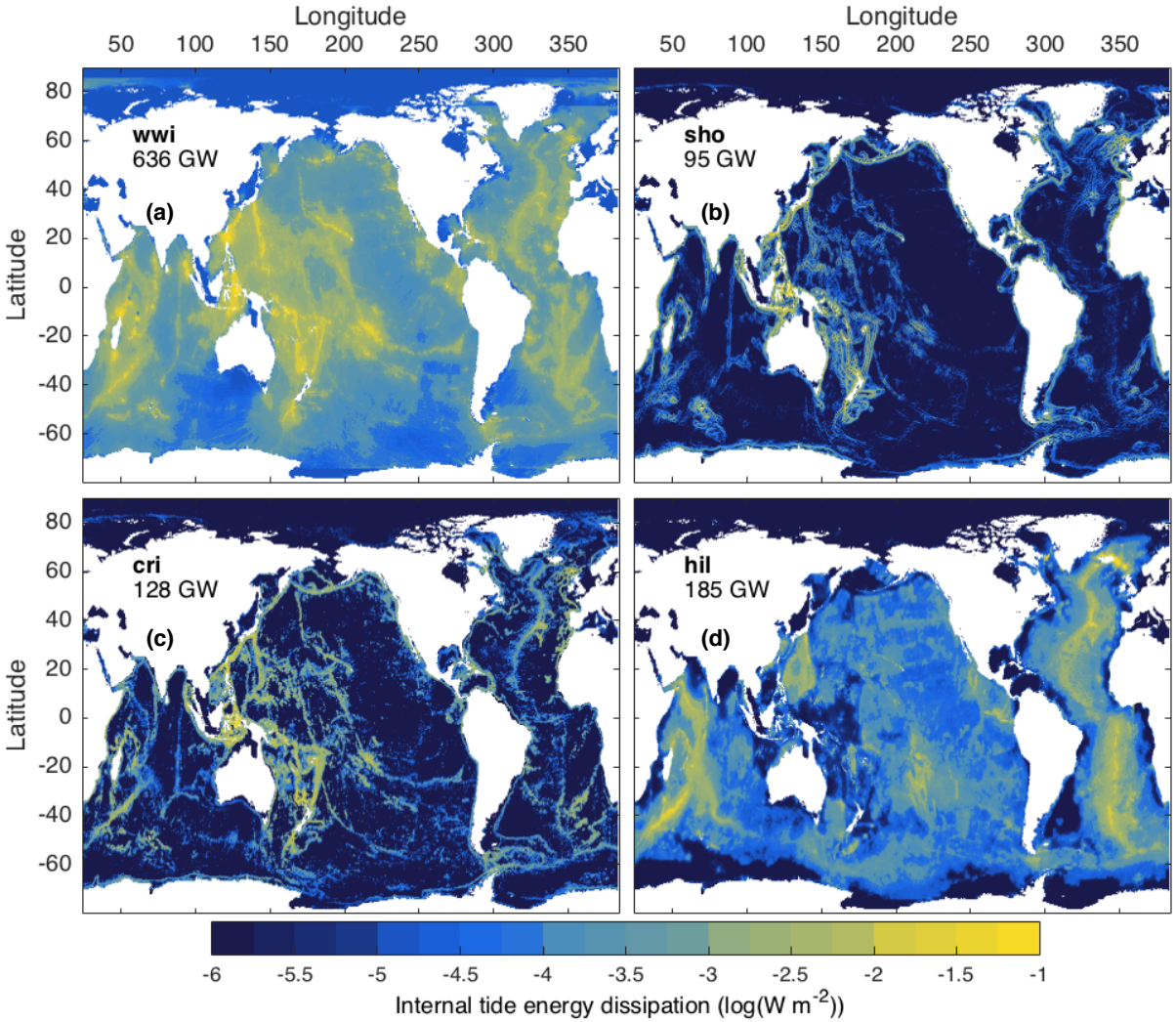

Figure 2: Global maps of the four static power fields that enter the parameterization.

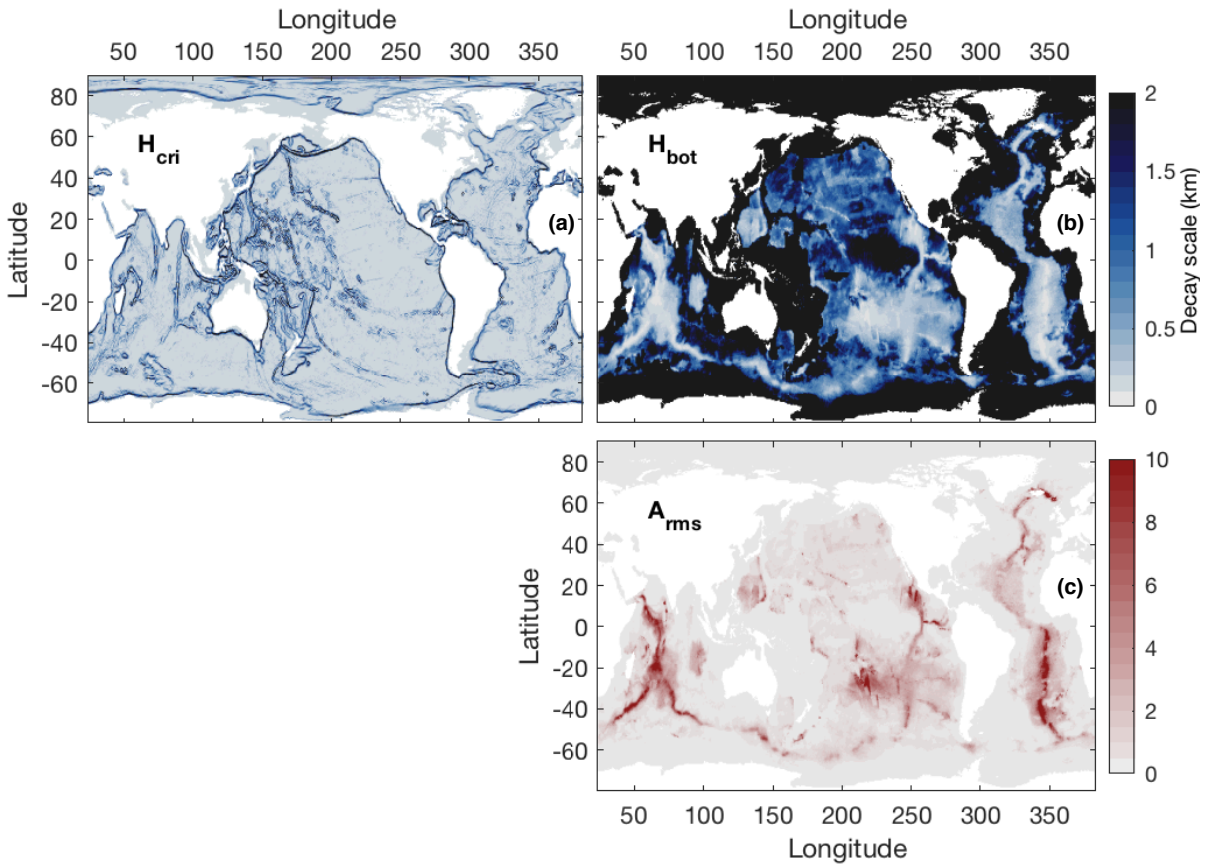

Figure 3: Global maps of the two decay scales, (a) H_{cri} and (b) H_{bot}, that enter the parameterization. Panel (c) shows A_{rms} normalized by its global average.

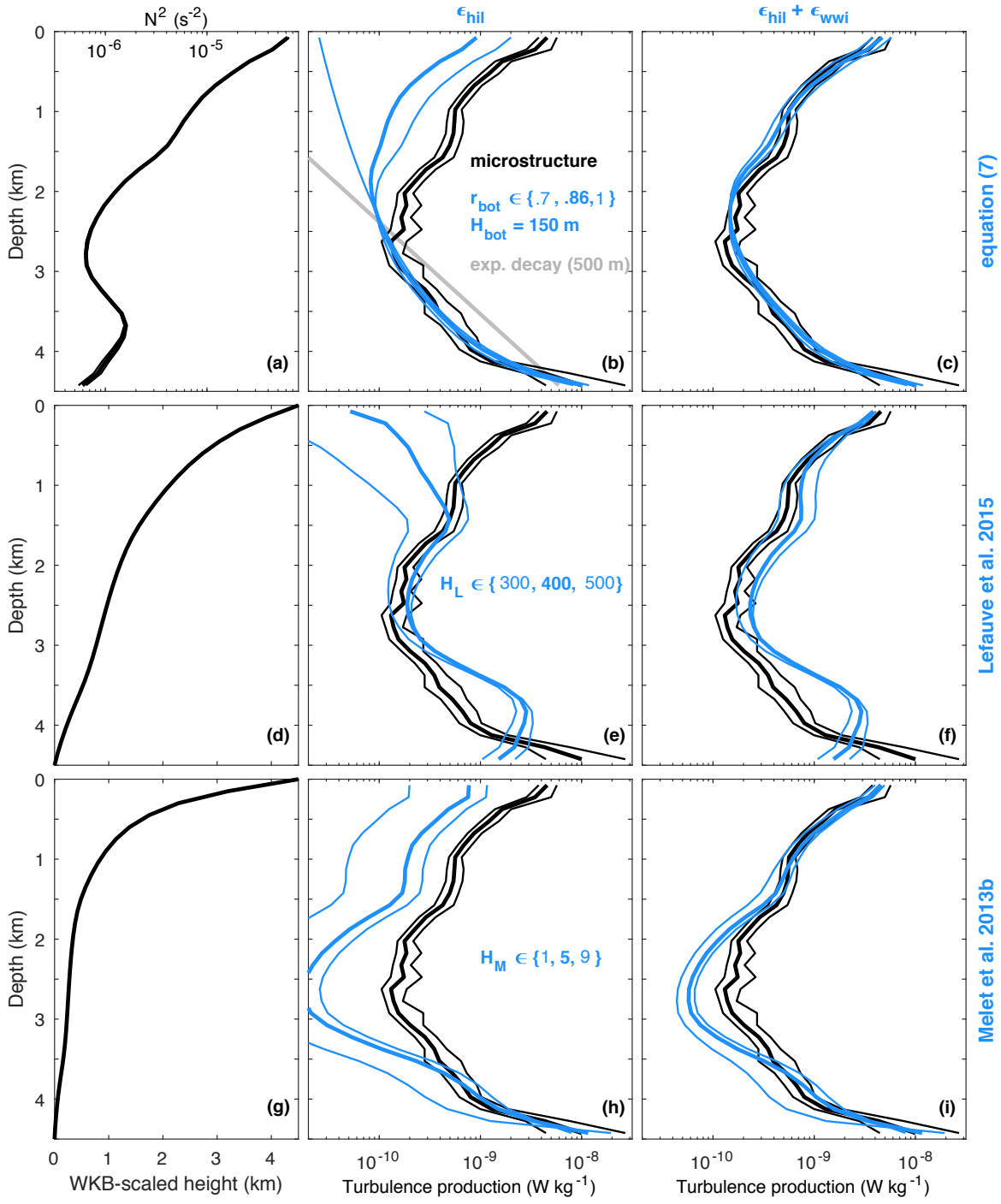

Figure 4: Parameterized dissipation in the eastern Brazil Basin (21-22°S; 16-19°W). (a) Composite stratification profile. (b) Composite microstructure profile (black) and parameterized ϵ_{hil} profile (blue) for H_{bot} = 150 m and three values of r_{bot}. An exponential decay with an e-folding scale of 500 m (St Laurent et al. 2002) is shown in grey. (c), Same as (b), with the total parameterized profile $\epsilon_{hil} + \epsilon_{wwi}$ in blue. (d) WKB-scaled height above bottom as defined by Lefauve et al. (2015) and applied to the composite stratification profile. (e,f), Same as (b,c), with ϵ_{hil} distributed according to Lefauve et al. (2015) and three values of H_L. (g) WKB-scaled height above bottom as defined by Melet et al. (2013b). (h,i), Same as (b,c), with ϵ_{hil} distributed according to Melet et al. (2013b) and three values of H_M. In all panels, thin black lines delimitate 95% confidence intervals from bootstrapping.

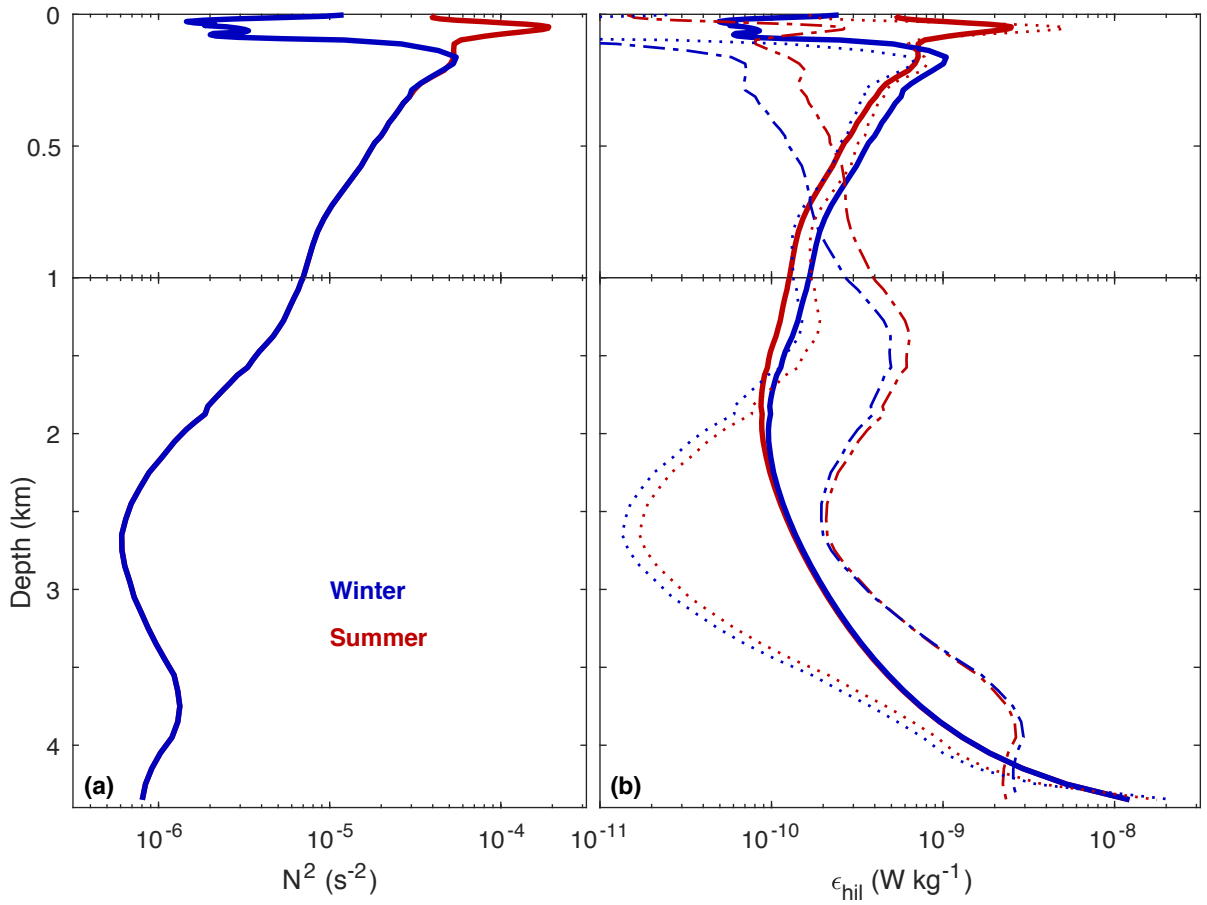

Figure 5: Seasonal change of parameterized turbulence production in the eastern Brazil Basin (21-22°S; 16-19°W). (a) Stratification profile representative of (blue) winter and (red) summer, from World Ocean Atlas 2018 (Locarnini et al. 2018, Zweng et al. 2018). (b) Parameterized ϵ_{hil} profile in (red) summer and (blue) winter. The present parameterization (H_{bot} = 150 m, $r_{bot} = 0.86$) is shown by thick lines. For comparison, we also show (dashed-dotted lines) the vertical structure of Lefauve et al. (2015) with H_L = 400 m and (dotted lines) that of Melet et al. (2013b) with H_M = 5 m.

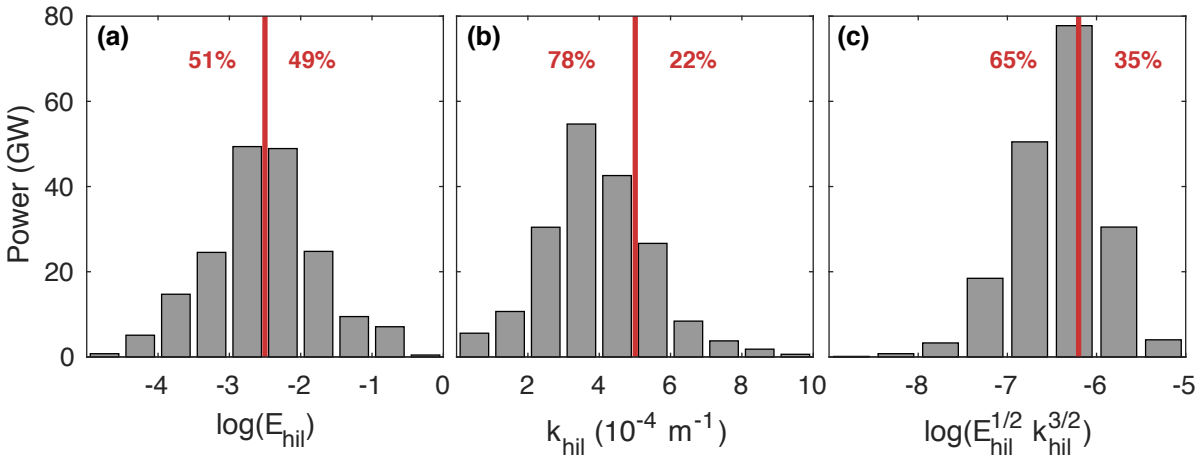

Figure 6: Distribution of the global total power, $\int\int E_{hil}\, dxdy$, as a function of (a) E_{hil}, (b) k_{hil} and (c) $E_{hil}^{1/2} k_{hil}^{3/2} \propto A_{rms}$. The red line shows the eastern Brazil Basin (21-22°S; 16-19°W) value.

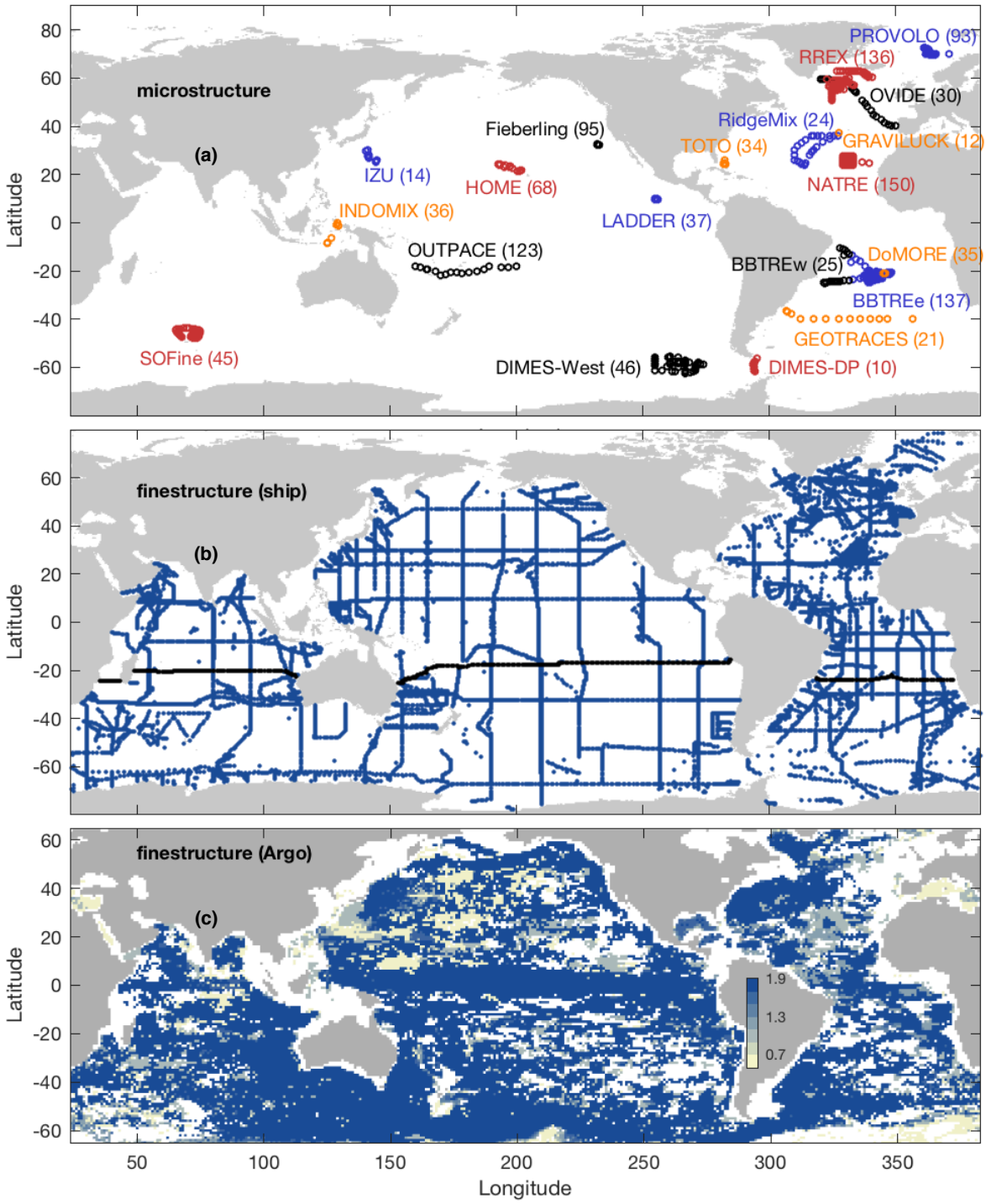

Figure 7: Global (a) microstructure, (b) ship-based finestructure (Kunze 2017) and (c) Argo-based finestructure (Whalen et al. 2015) sampling. The number of profiles for each project is shown in parentheses in (a). Finestructure profile locations are shown in blue and black in (b); black sections are those plotted in Figs. 13, S1 and S2. Shading in (c) depicts the maximum depth (in kilometres) of Argo-based finestructure profiles.

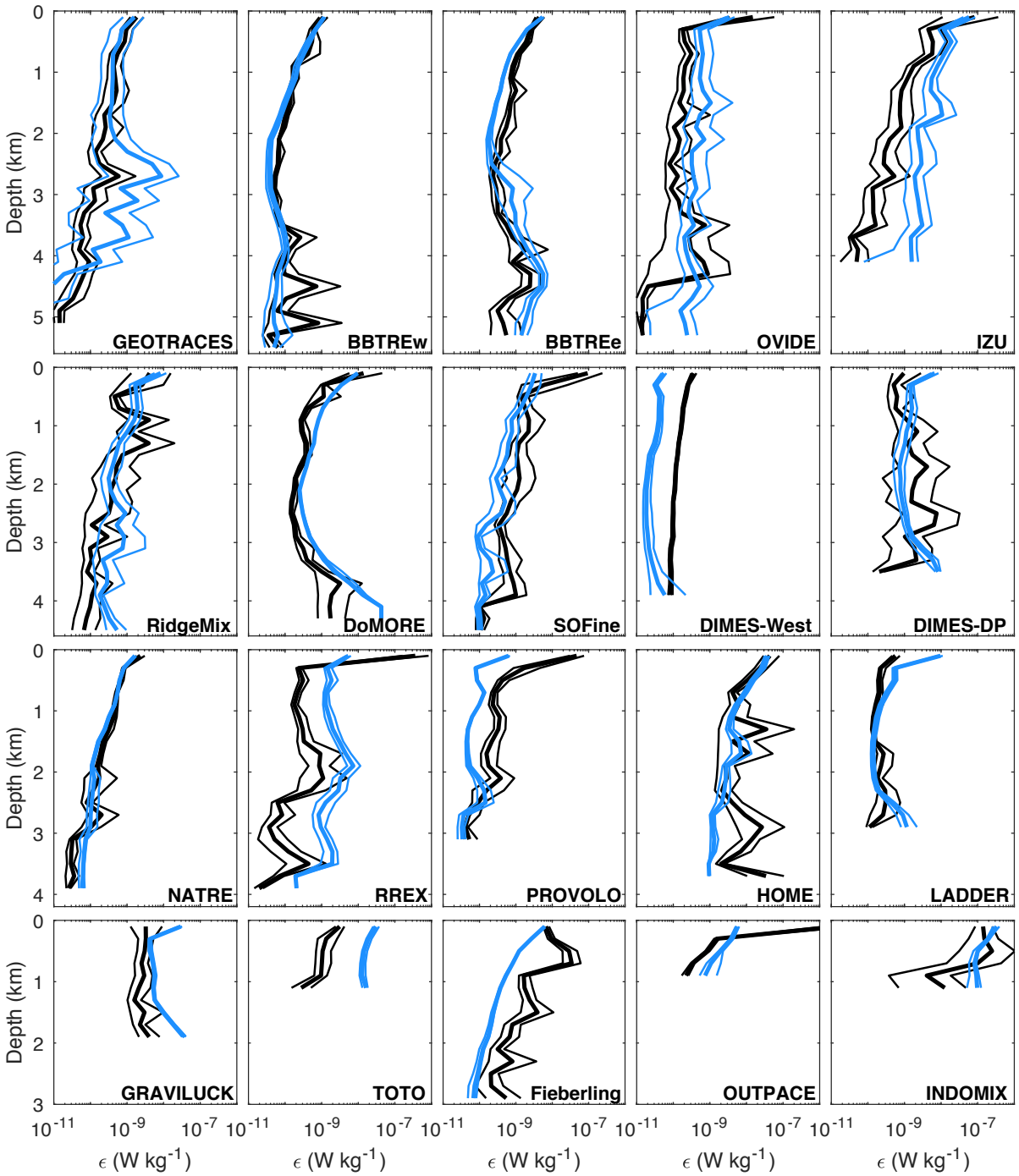

Figure 8: Project-average microstructure profiles (black) compared to parameterized profiles (blue). Parameterized profiles are obtained by sampling the global distribution of internal tide energy dissipation—which is based on the WOCE climatology of stratification—at the location and depths of each available microstructure profile. If either the parameterized or measured profile is not defined at some depth, both are set to not-a-number at this depth before taking the average; this ensures that differences in coverage do not bias the comparison. Thin lines delimitate 95% confidence intervals from bootstrapping. Project locations are shown in Fig. 7.

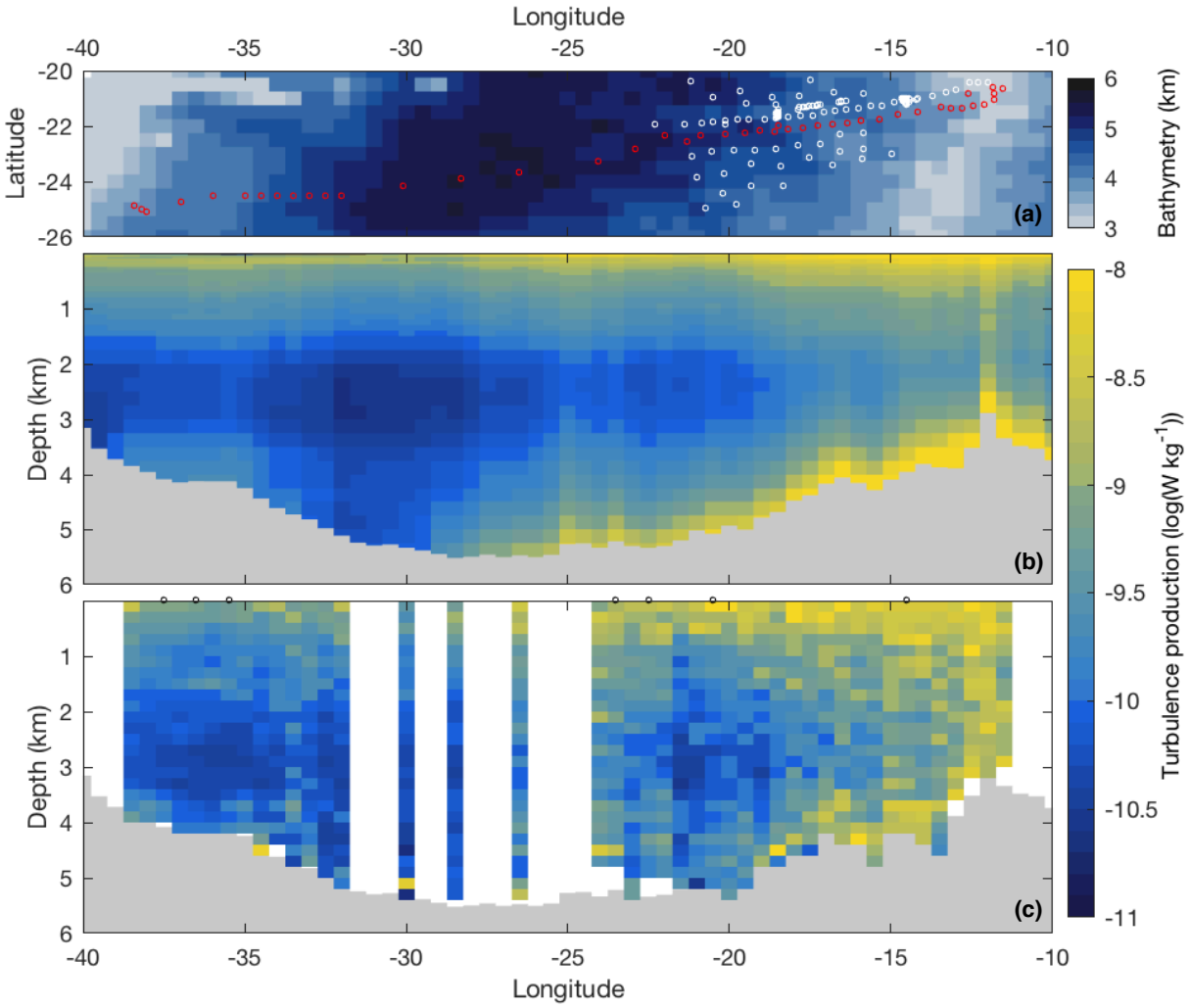

Figure 9: Southwestern Atlantic transect of (b) parameterized and (c) measured turbulence production. Selected measurements are BBTRE microstructure profiles shown in red in (a). Selected grid points for the parameterization track the observational transect. Horizontal linear interpolation has been used in seven unsampled grid columns (marked by circles) of panel (c). Shading in (a) shows the 'etopo2v2' bathymetry (Smith and Sandwell 1997) averaged at 0.5° resolution.

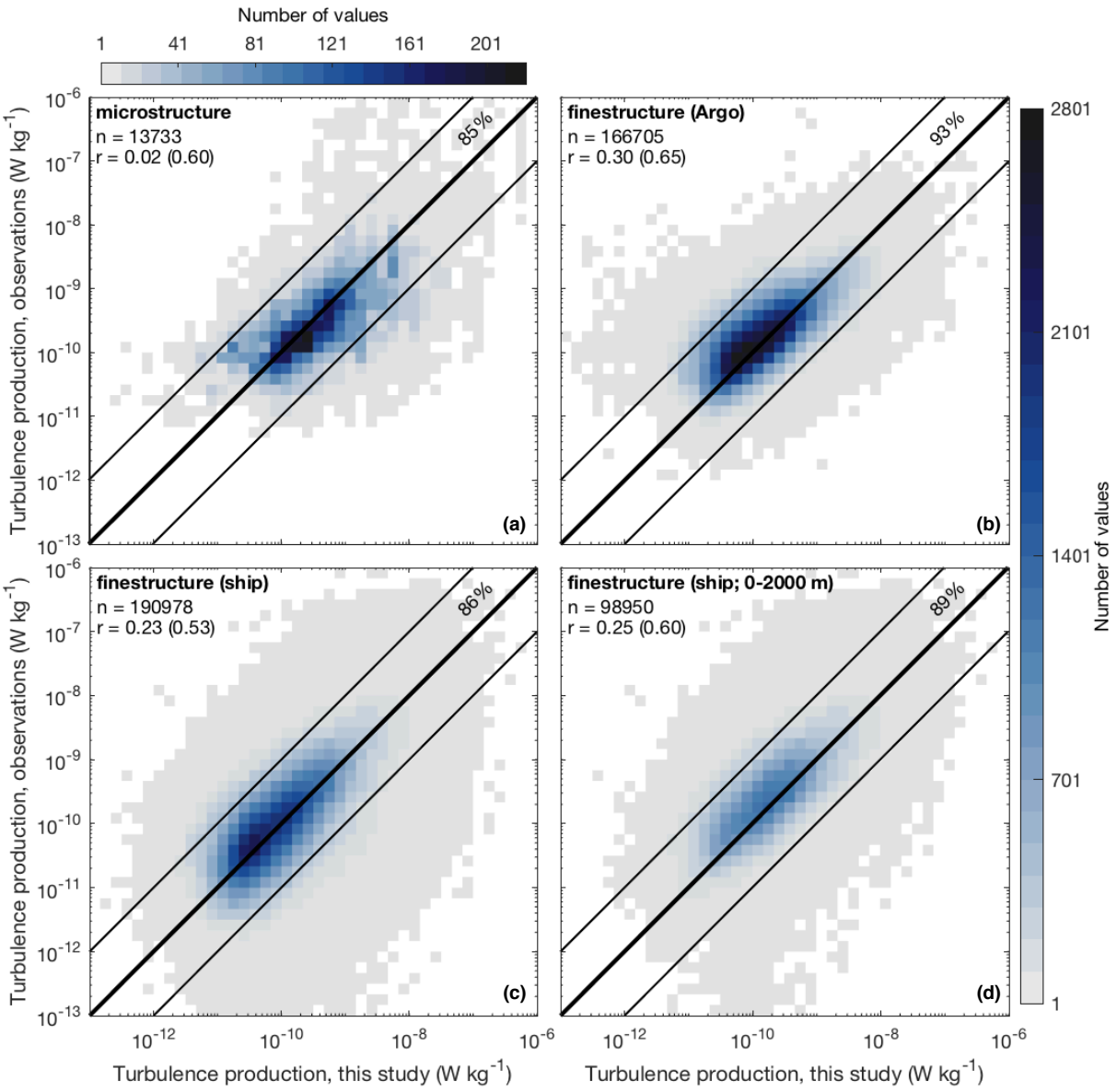

Figure 10: Turbulence production estimated from (a) microstructure or (b-d) finestructure observations (y-axis) versus that predicted by the present parameterization (x-axis). Panel (b) uses the dataset of Whalen et al. (2015). Panels (c,d) use the dataset of Kunze (2017), with depths > 2 km excluded in panel (d). Colourscales show the number of values in each dissipation bin; one value corresponds to one 200 m profile segment. The top colourscale applies to panel (a); the right-side colourscale applies to other panels. Total number of values (n) and correlation coefficients (r) are given in the top-left corner of each panel; outside (inside) parentheses is the correlation coefficient computed using raw (using the logarithm of) dissipation values. All correlations are statistically significant (p-value < 0.05). Thin black lines delimitate agreement within a factor of 10; the corresponding percentage of values is given at the top right of each panel.

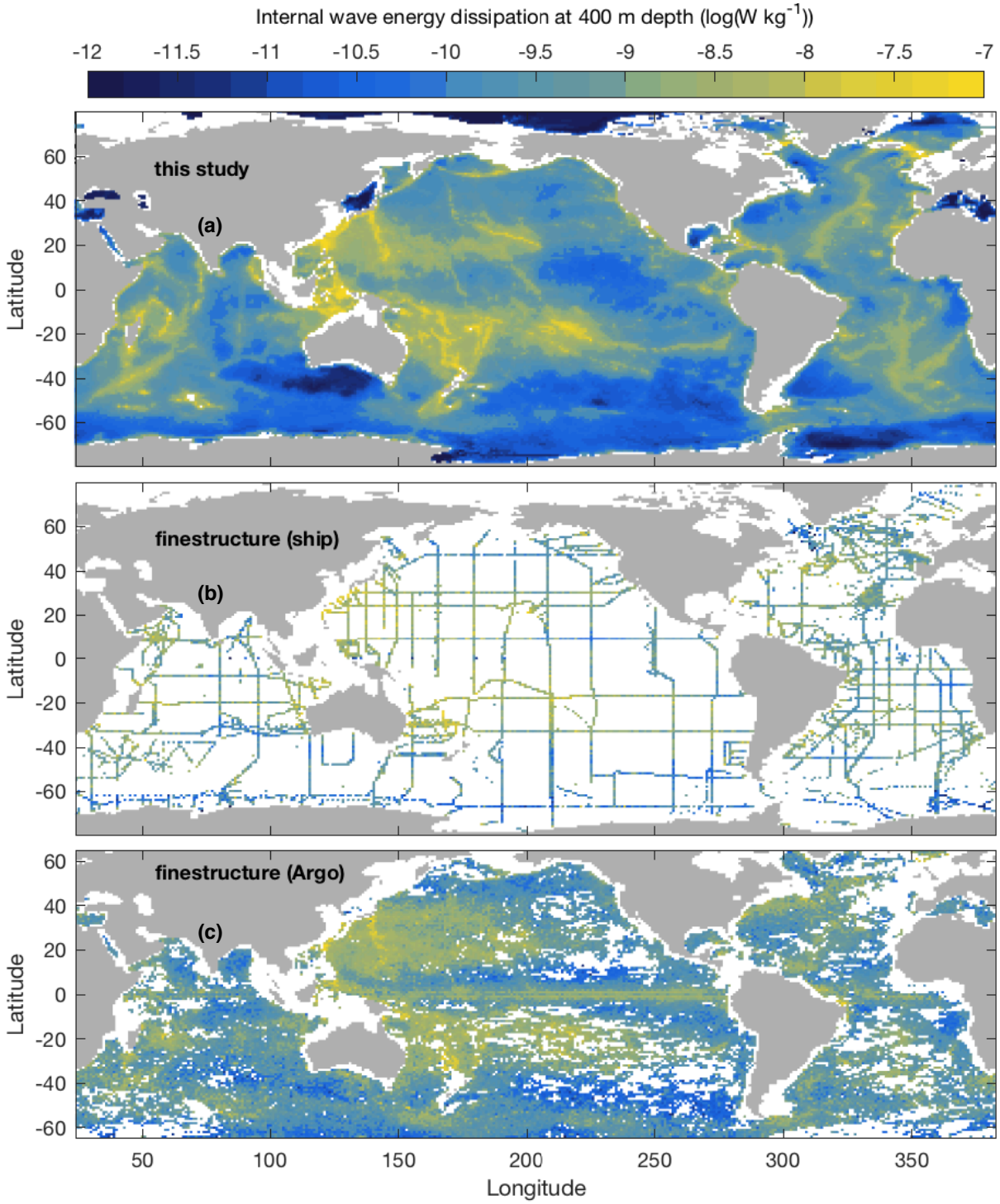

Figure 11: Internal wave energy dissipation at 400 m depth predicted from (a) the present parameterization, (b) ship-based finestructure observations (Kunze 2017) and (c) Argo-based finestructure observations (Whalen et al. 2015).

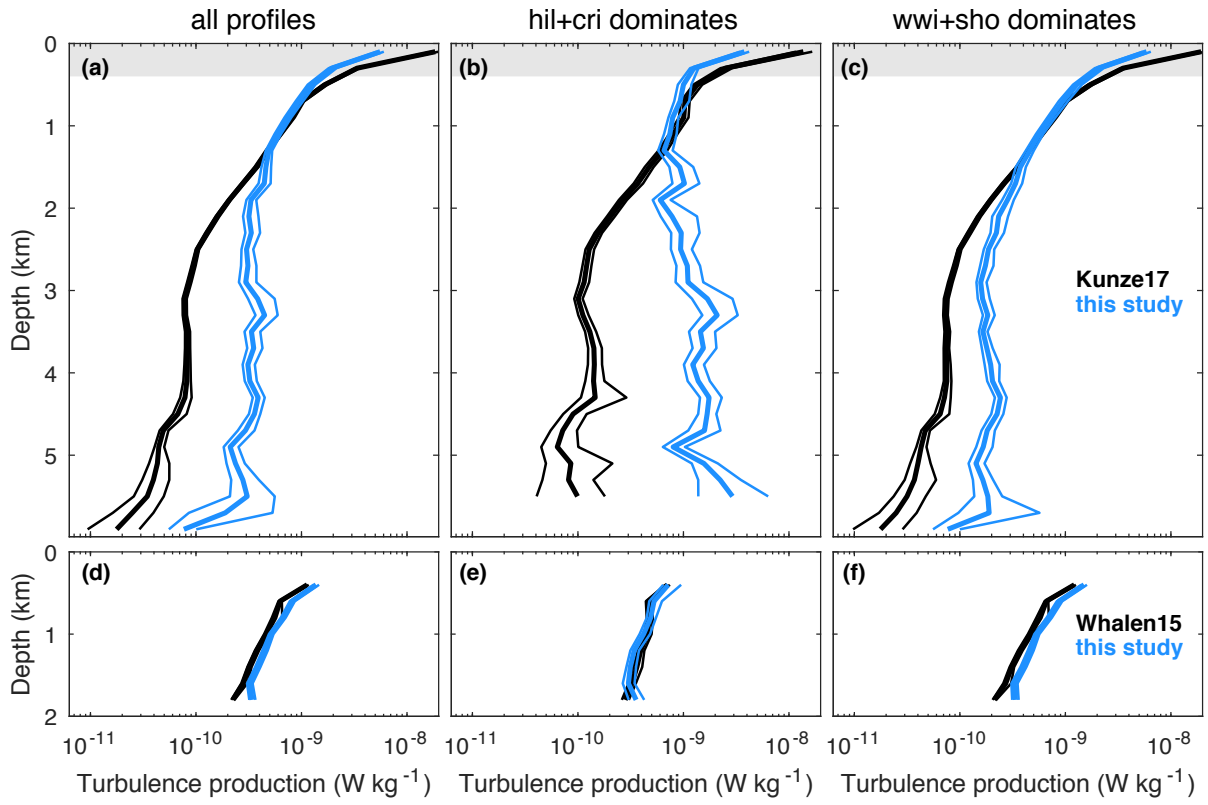

Figure 12: Average (black) finestructure-inferred and (blue) parameterized turbulence production profile. Parameterized profiles are obtained by sampling the global distribution of dissipation at the location and depths of each available finestructure profile. (a,d) All profiles. (b,e) Profiles where $E_{cri} + E_{hil} > E_{wwi} + E_{sho}$. (c,f) Profiles where $E_{cri} + E_{hil} < E_{wwi} + E_{sho}$. Panels (a-c) use the finestructure dataset of Kunze (2017); panels (d-f) use that of Whalen et al. (2015). Thin lines delimitate 95% confidence intervals from bootstrapping. Grey shading in (a-c) marks the 0-380 m depth range within which finestructure estimates were deemed unreliable by Kunze (2017).

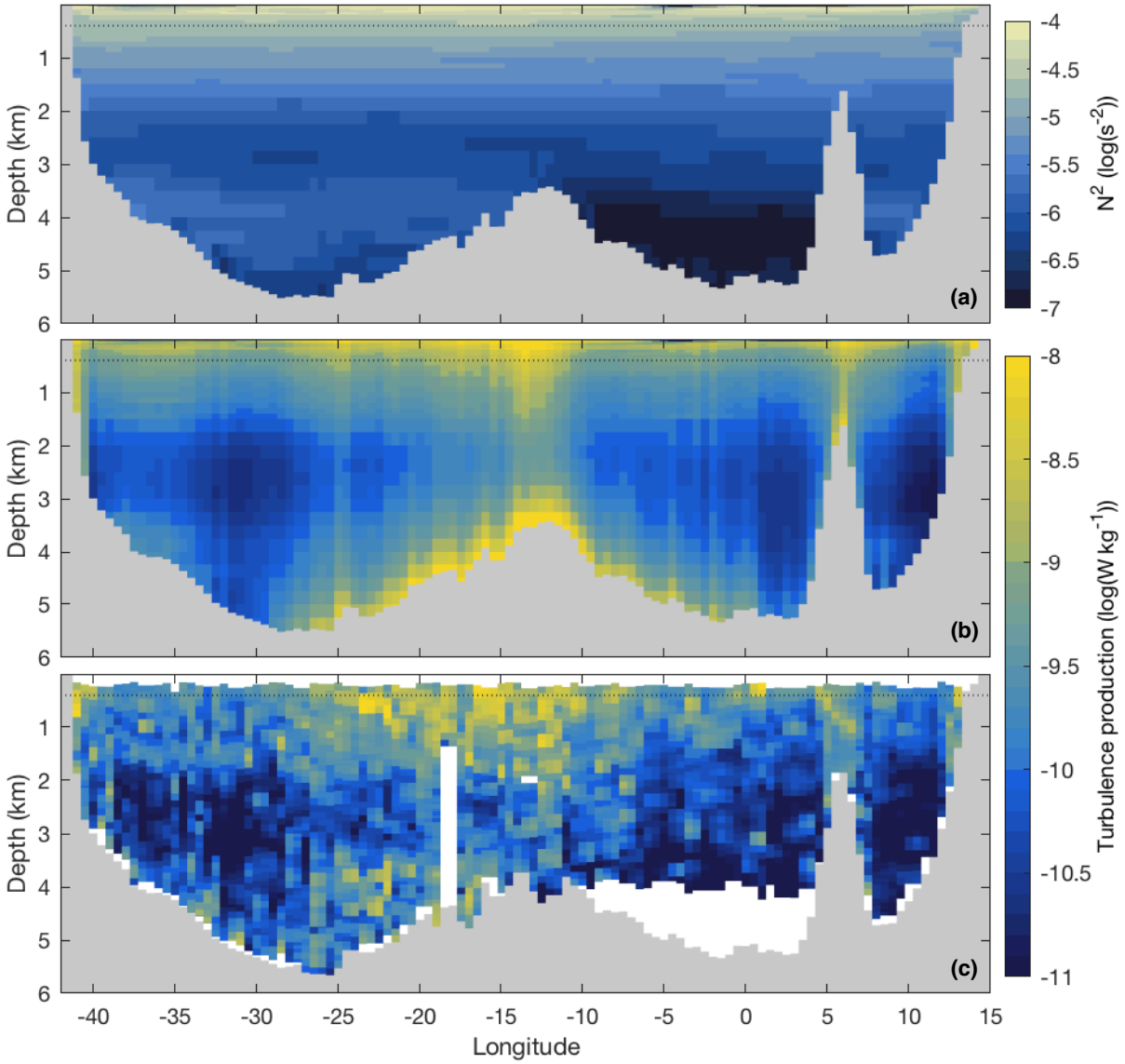

Figure 13: South Atlantic transect, near 23°S, of (a) climatological stratification, (b) parameterized turbulence production and (c) finestructure-inferred turbulence production (Kunze 2017). Transect location is shown in Fig. 7b.

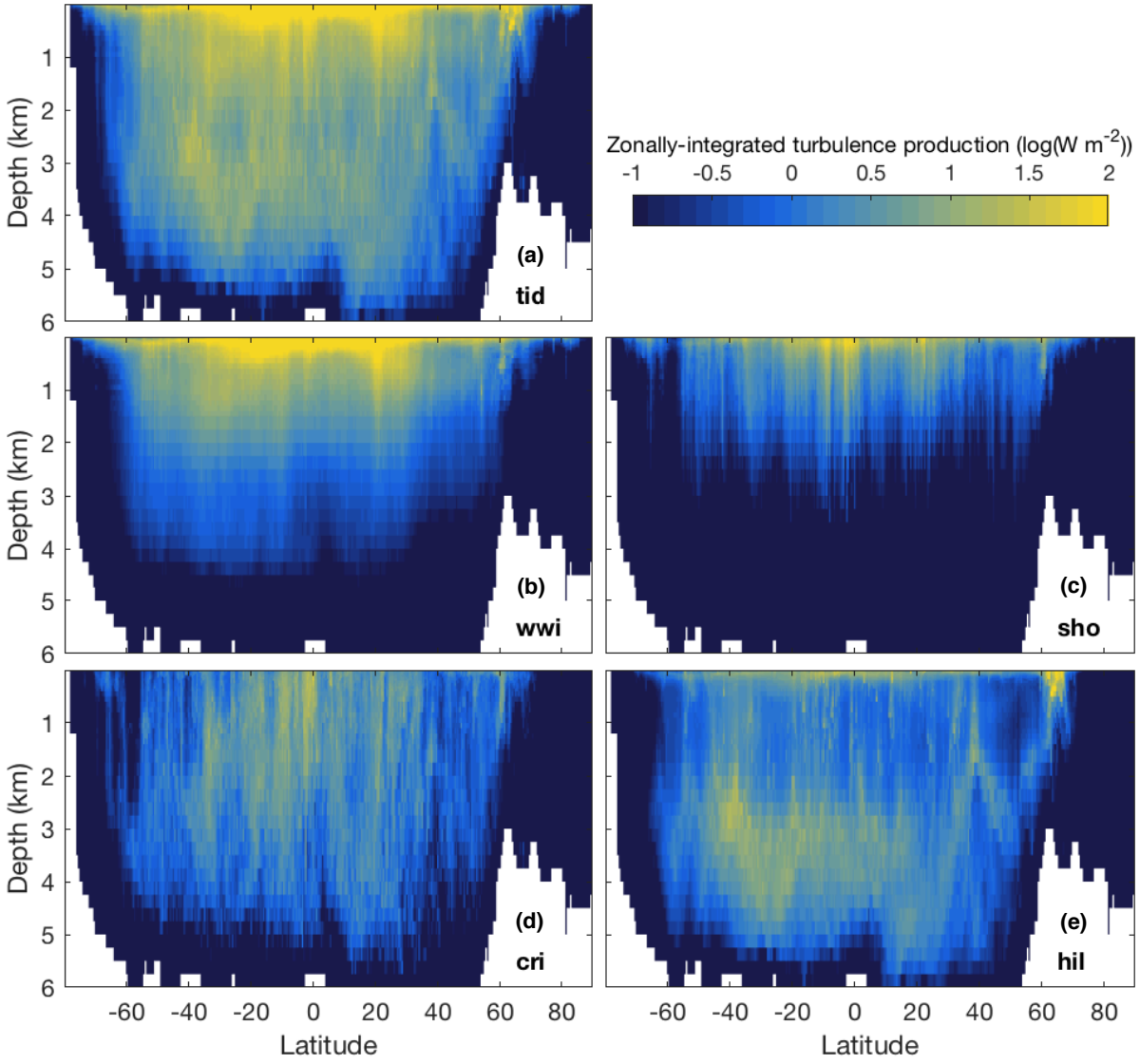

Figure 14: Global zonal sum of (a) the total turbulence production ϵ_{tid} and (b-e) its decomposition into the four components: (b) ϵ_{wwi}, (c) ϵ_{sho}, (d) ϵ_{cri} and (e) ϵ_{hil}.

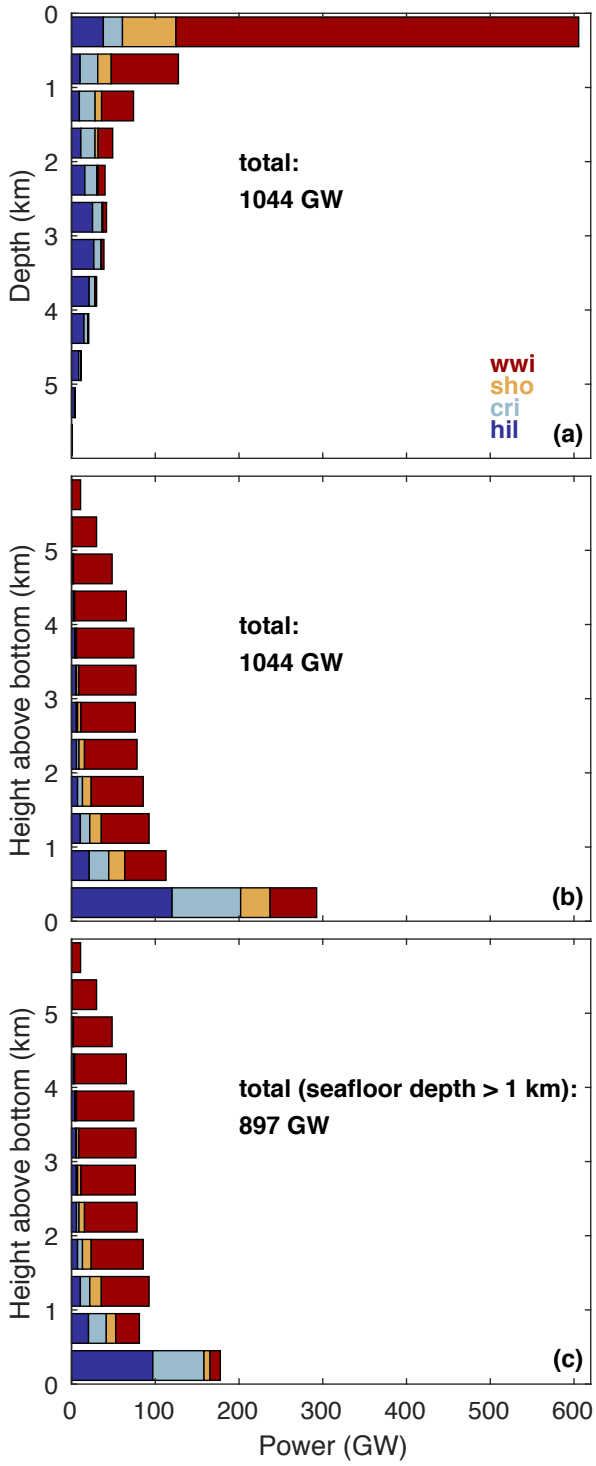

Figure 15: Global distribution of ϵ_{tid} as a function of (a) depth and (b,c) height above bottom. Colors indicate respective contributions of (red) ϵ_{wwi}, (orange) ϵ_{sho}, (light blue) ϵ_{cri} and (blue) ϵ_{hil}. In panel (c), regions where the seafloor depth is less than 1 km have been excluded.

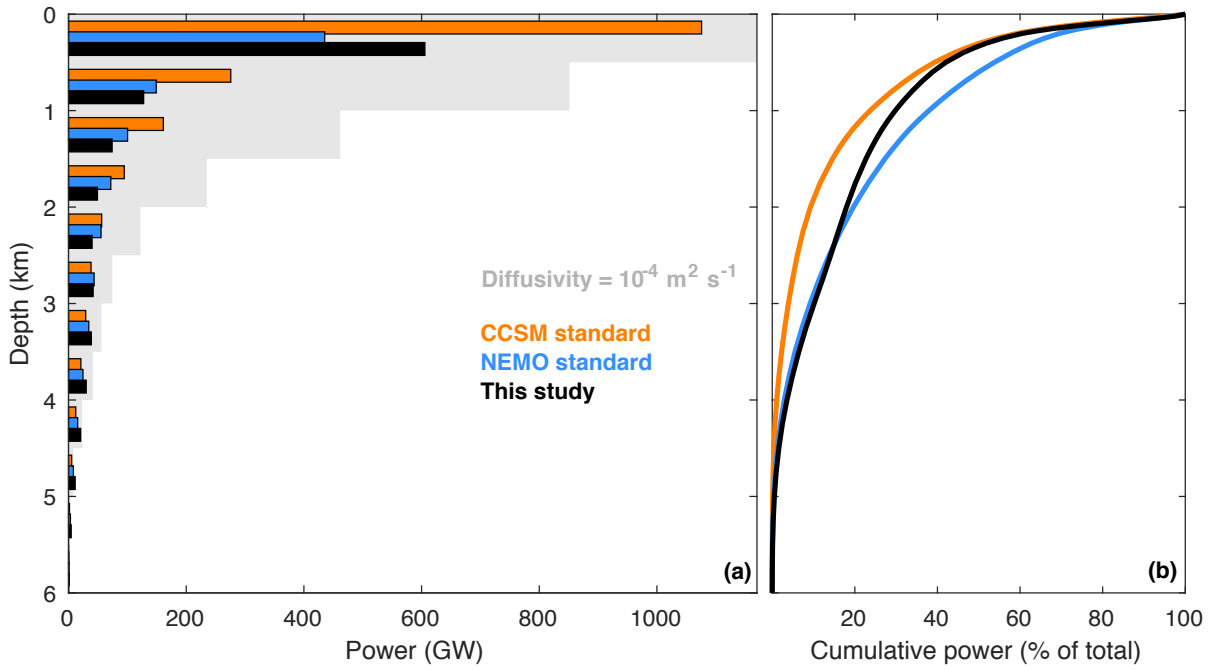

Figure 16: Global depth distribution of ϵ_{tid} in (black) this study, (blue) the standard NEMO parameterization and (orange) the standard CCSM parameterization. (a) Total turbulence production binned into 500 m depth intervals. The grey shading indicates turbulence production implied by a uniform diffusivity of 10^{-4} m^2 s^{-1}. (b) Cumulative turbulence production, given as a percentage of the global total.

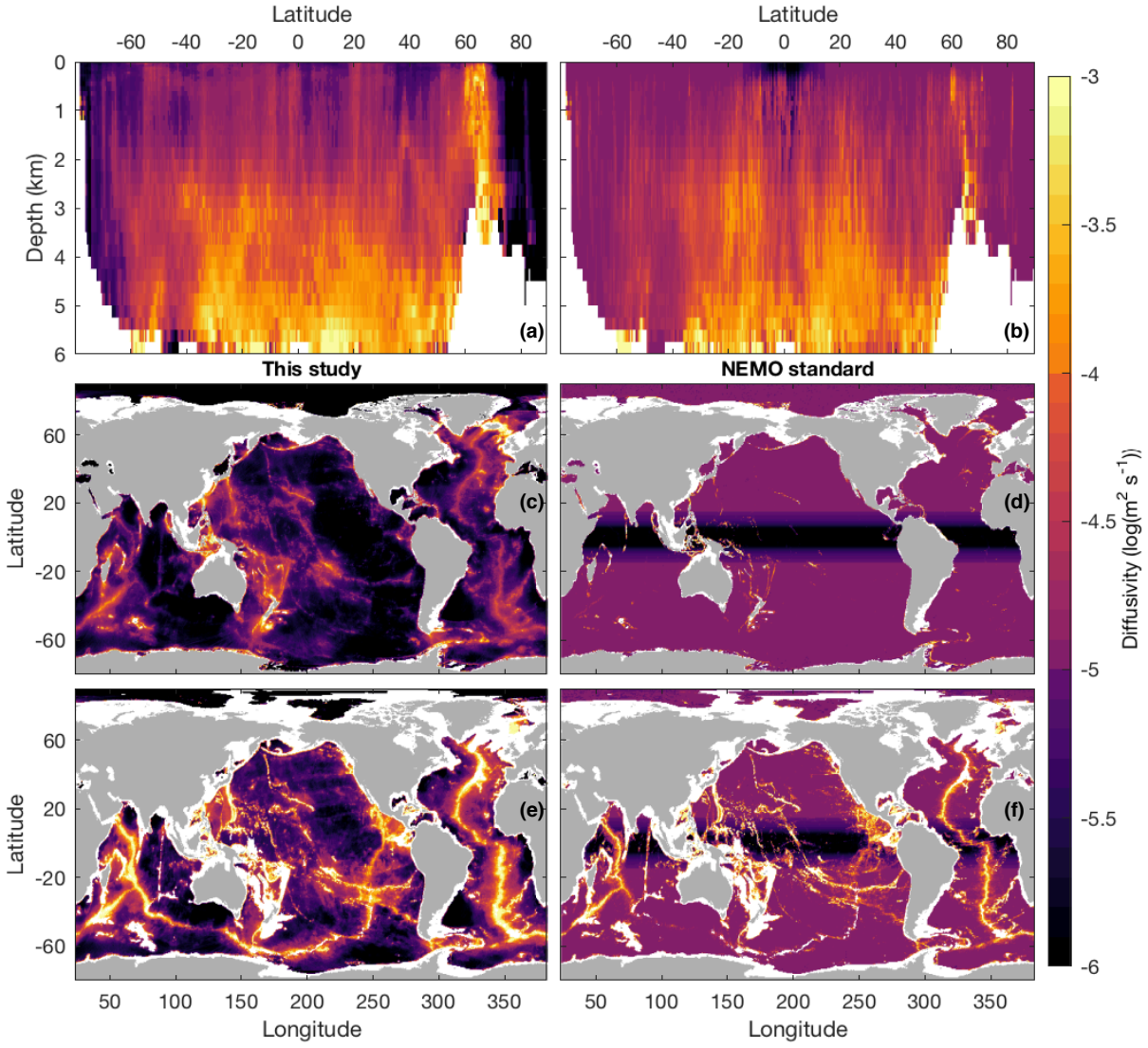

Figure 17: Diapycnal diffusivity in the present (a,c,e) and NEMO standard (b,d,f) mixing parameterizations. (a,b) Zonal mean diffusivity. (c,d) Diffusivity at 500 m depth. (e,f) Diffusivity at 3000 m depth. In panels (a,b) diffusivity averages have been weighted by N^2. Note that the standard NEMO parameterization also includes a reduction of diffusivity under sea ice and an elevation in Indonesian seas that are not represented here.

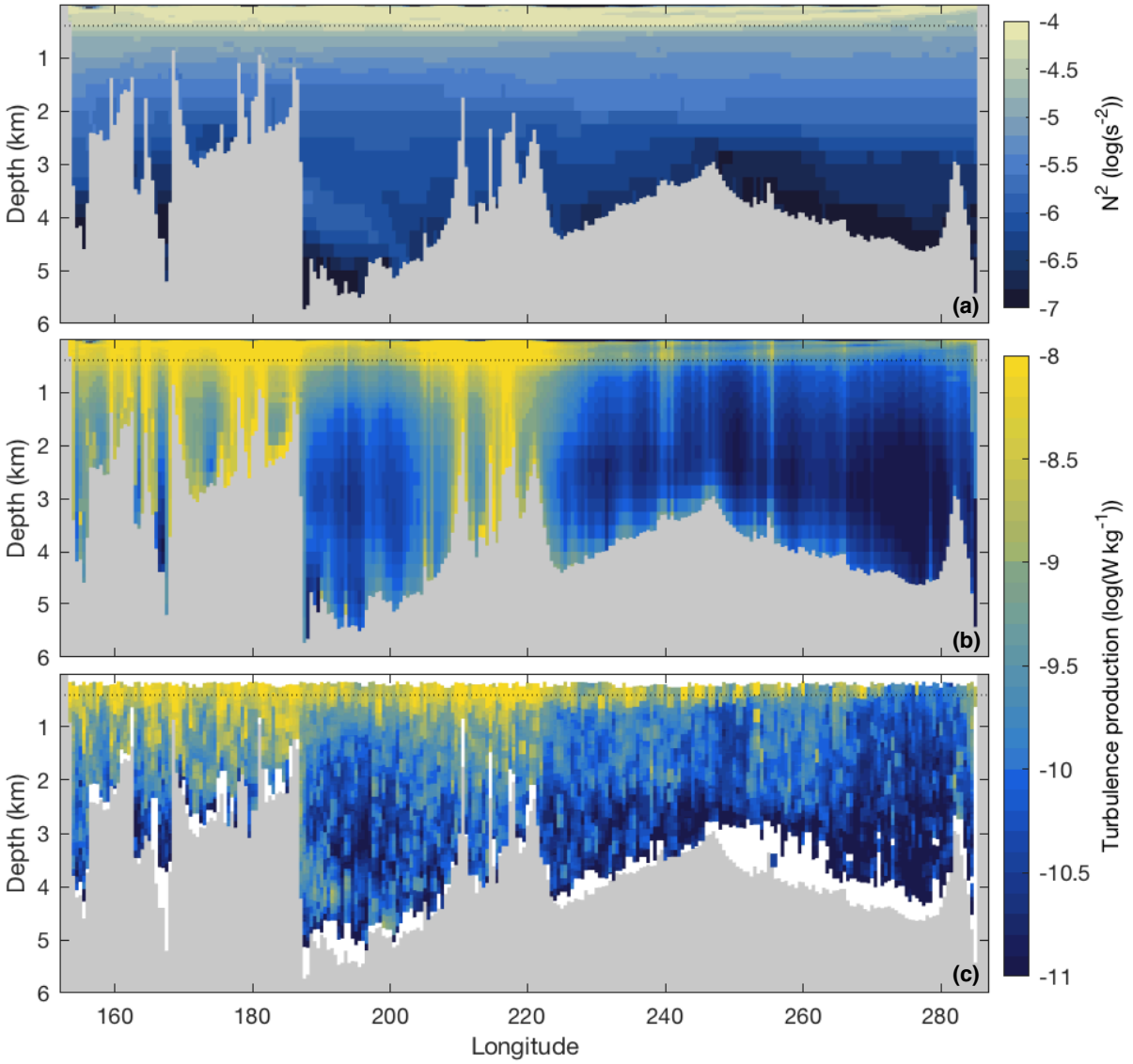

Figure S1: South Pacific transect (P21, near 17°S) of (a) climatological stratification, (b) parameterized turbulence production and (c) finestructure-inferred turbulence production (Kunze 2017). Transect location is shown in Fig. 7b.

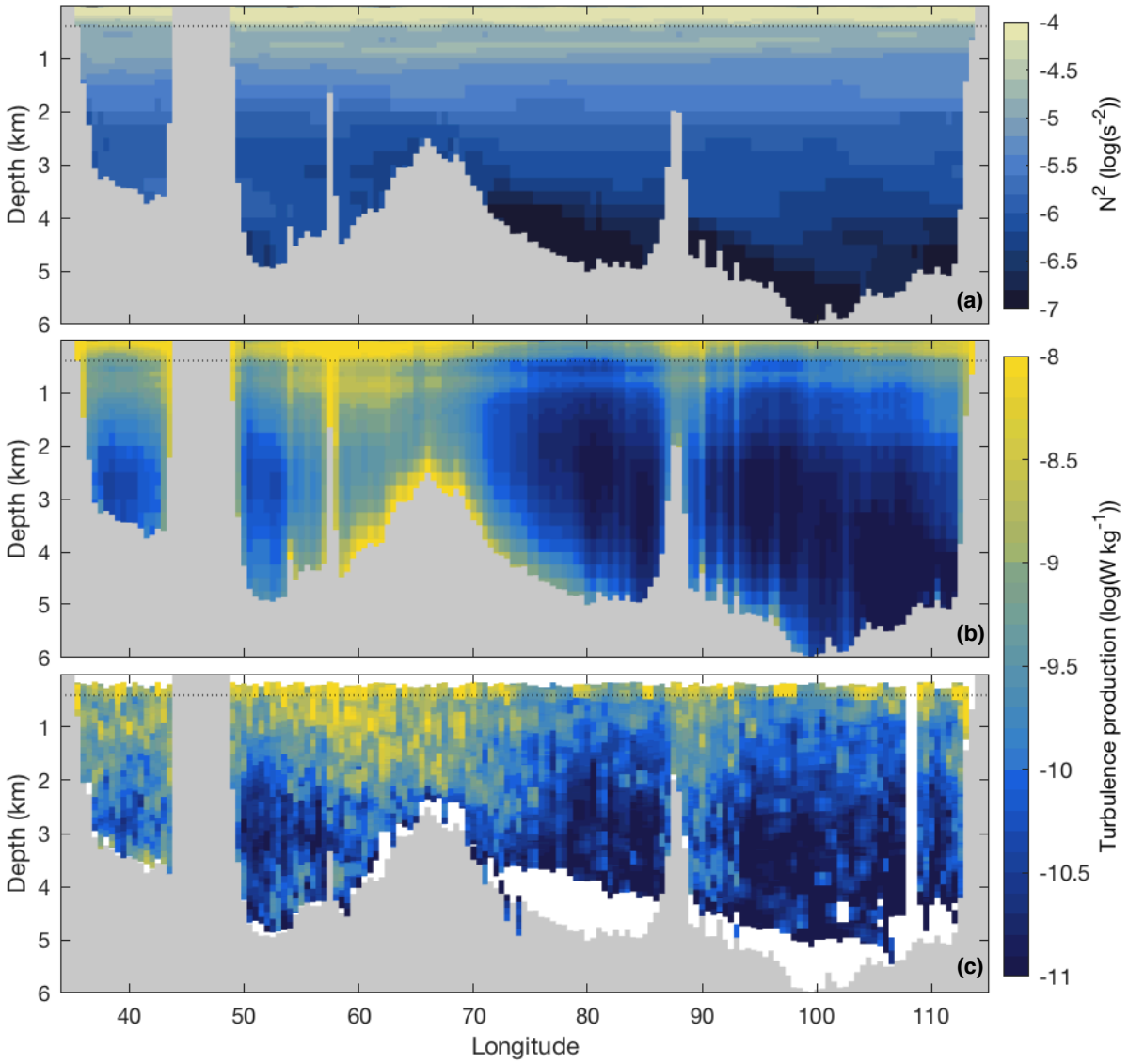

Figure S2: Indian Ocean transect (I03 and I04, near 20°S) of (a) climatological stratification, (b) parameterized turbulence production and (c) finestructure-inferred turbulence production (Kunze 2017). Transect location is shown in Fig. 7b.

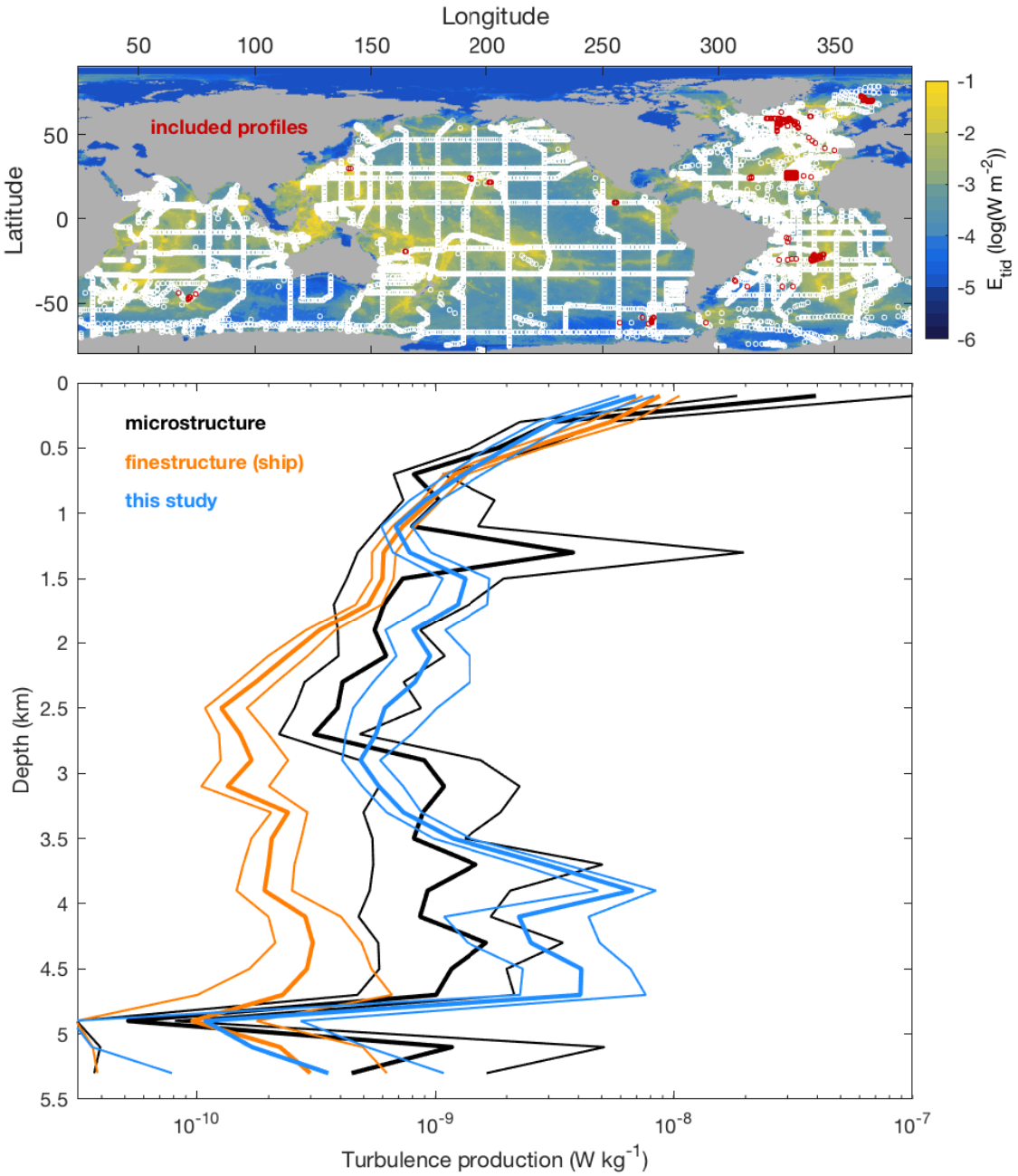

Figure S3: Comparison of turbulence production (black) measured by microstructure probes, (orange) inferred by Kunze (2017) and (blue) parameterized here. We first averaged finestructure and parameterized profiles located within 50 km of each microstructure cast. We thus obtained 540 profiles with defined microstructure, finestructure and parameterized values. If either of the three measures of dissipation is not defined at some depth, all three are set to not-a-number at this depth; this ensures that differences in coverage do not bias the comparison. Thick lines show the average over the 540 profiles. Thin lines enclose 95% confidence intervals from bootstrapping. The top panel shows in red the locations of the 540 profiles and in white the locations of all ship-based finestructure profiles, overlain on the shaded internal tide energy dissipation E_{tid}.